

Moving Target Artifacts in Bistatic Synthetic Aperture Radar Images

Kaan Duman, *Student Member, IEEE*, and Birsen Yazıcı, *Senior Member, IEEE*

Abstract—Synthetic aperture radar (SAR) imaging methods are designed to image stationary scenes. Moving targets appear smeared and misplaced in reconstructed SAR images. This paper presents a theory to quantitatively analyze and predict positioning errors due to moving targets in bistatic SAR imagery. We derive closed-form, parametric equations between the target velocities and positioning errors in reconstructed images. The analysis is applicable to scenarios involving bistatic configurations and arbitrary imaging geometries including arbitrary antenna trajectories, target velocities, and nonflat topography. We present examples for specific geometric configurations including straight linear trajectories and short and long apertures in bistatic configurations. The predictive equations offer the potential capability to extract moving target signatures, estimate target motion parameters, and form focused bistatic SAR images in complex imaging geometries.

Index Terms—Bistatic synthetic aperture radar (SAR), moving target imaging, moving target morphology, positioning errors due to moving targets.

I. INTRODUCTION

SYNTHETIC Aperture Radar (SAR) image formation methods are designed to match the phase of the measured data to that of a stationary target over a coherent processing interval (CPI). However, the range and spatial Doppler of a moving target differ from those of a stationary one over a CPI, resulting in a mismatch. This mismatch causes the smearing and displacement of moving targets in SAR images. In this paper, we present a theory to predict and quantify moving target positioning errors in bistatic SAR imagery. The analysis is applicable to arbitrary imaging geometries including arbitrary antenna trajectories and velocities, non-flat topography, wide apertures and nonlinear wavefront curvatures. To the best of our knowledge, our study is the first to provide a comprehensive quantitative analysis of moving target positioning errors for the bistatic configuration and arbitrary imaging geometries.

Our analysis is based on backprojection-based (BP-based) imaging although results are applicable to other image reconstruction methods. BP-based methods have many advantages over the range-Doppler or Fast Fourier Transform

(FFT) based image formation methods. These include the ability to handle wide-aperture data, the ability to accommodate arbitrary imaging geometries and wavefront curvatures, adaptability of the reconstruction algorithms to different SAR modalities [1]–[14], and computational efficiency among others [15].

We use microlocal analysis, an abstract theory of generalized Radon transforms [16], as an underlying framework. Our analysis provides analytic, closed-form parametric equations between the three-dimensional target velocity and two-dimensional positioning errors. More specifically, these equations depend on target position and range, target velocity, antenna trajectories, bistatic angle and slow-time, providing general expressions that can predict and explain moving target morphology due to nonlinear motion in SAR imaging. The analysis is applicable to bistatic and monostatic configurations, multiple and extended moving targets, and arbitrary imaging geometries including arbitrary antenna trajectories and target velocities. In addition to the general analysis, we consider specific bistatic configurations involving straight linear trajectories, constant antenna velocity, wide and short aperture cases. Extensive numerical simulations demonstrate the validity of the theory for different geometries, configurations and target velocities.

A. Related Work

The effects of moving targets in SAR imagery have been studied in a number of papers [17]–[22]. These papers consider a monostatic antenna traversing a straight, linear trajectory at a constant height and a constant velocity over a flat topography. In [17] moving target effects in range-migration images are quantified in radial and cross-range directions in terms of target velocities. The study concludes that the majority of smearing and defocusing artifacts occurs in the cross-range direction. In [18] similar results are derived in the wavenumber domain for the BP-based SAR imagery. In [19] and [20] quantitative relationships between the target positioning error and the relative target-to-radar velocity are derived for BP-based SAR imagery. The results in [20] are extended to multichannel SAR imagery in [21]. In [22] moving target artifacts are analyzed in the spotlight mode SAR imaging when targets undergo nonlinear motion. Closed form equations for the positioning errors in subapertures are presented.

The analysis of moving target artifacts and SAR moving target imaging tasks are interrelated, as any moving target imaging method requires an understanding of motion parameters and moving target artifacts. In the past two decades,

Manuscript received December 09, 2014; revised March 14, 2015; accepted May 14, 2015. Date of publication June 03, 2015; date of current version June 26, 2015. This work was supported in part by the Air Force Office of Scientific Research (AFOSR) under the agreement FA9550-12-1-0415 and in part by the National Science Foundation (NSF) under Grant CCF-08030672 and Grant CCF-1218805. The associate editor coordinating the review of this manuscript and approving it for publication was Prof. Edwin Marego.

The authors are with the Department of Electrical, Computer, and Systems Engineering, Rensselaer Polytechnic Institute, Troy, NY 12180 USA (e-mail: dumank@rpi.edu; yazici@ecse.rpi.edu).

Color versions of one or more of the figures in this paper are available online at <http://ieeexplore.ieee.org>.

Digital Object Identifier 10.1109/TCl.2015.2440995

several SAR moving target detection and imaging methods have been developed [1]–[4], [7], [20], [23]–[42]. From the perspective of the current study, these methods can be classified into two categories. The first category of methods explicitly use quantitative positioning error analysis and develop target detection and focusing methods [23]–[26]. In [23]–[25] moving target detection and imaging methods were developed under the assumption that the motion induced smearing lies in the radar cross-range direction alone. In [26], the results in [19] were used to develop SAR focusing methods.

The second category of methods are based on spectral signatures of moving targets or generalized likelihood ratio test (GLRT) type methods. This class includes autofocus type methods [27], [35], the keystone transform based methods [23], [34], time-frequency transform based methods [29], [30], inverse synthetic aperture imaging type methods [36]–[38], and GLRT type methods in which the reflectivity images are formed for a range of hypothesized motion parameters while simultaneously estimating the unknown motion parameters [1]–[4], [27], [31], [33], [39], [43].

B. Advantages of Our Work

(i) Our analysis and results are applicable to bistatic configuration and arbitrary imaging geometries including arbitrary antenna trajectories, speed, non-flat topography, long and short apertures. Consequently, the results can be used to develop methods for detecting moving targets, focusing bistatic SAR images and suppressing artifacts in arbitrary imaging geometries and bistatic configurations. (ii) The analysis is applicable to extended targets and nonlinear target and antenna motion; hence, it can explain complex moving target morphology in SAR imagery. (iii) The analysis does not rely on limiting assumptions such as short aperture, small scene or linear wavefront curvature. (iv) The analysis is based on microlocal analysis [16]. Therefore, the underlying methodology is general and can be used to analyze moving target positioning errors in other SAR modalities [1]–[4], [8]–[11], [40].

C. Organization of the Paper

The paper is organized as follows: in Section II we present the bistatic SAR forward model and BP-based image formation method for moving targets. In Section III, we derived the criticality conditions that describe the propagation of visible edges of a scene to a bistatic SAR image. In Section IV, we use the criticality conditions presented in the previous section to derive analytic equations representing moving target positioning errors in bistatic SAR imagery for arbitrary imaging geometries. In Section V, we focus on specific bistatic and monostatic SAR geometries and express the analytic equations derived in the previous section in terms of the underlying parameters of these geometries. In Section VI, we present numerical simulations. Section VII concludes the paper.

II. THE FORWARD MODEL AND BACKPROJECTION-BASED IMAGE FORMATION FOR BI-SAR MOVING TARGET IMAGING

In this section, we present the forward model and the backprojection-based reflectivity image reconstruction method when the scene of interest includes moving targets.

We use the following notational conventions throughout the paper. The bold Roman, bold italic and Roman lower-case letters are used to denote variables in \mathbb{R}^3 , \mathbb{R}^2 and \mathbb{R} , respectively, i.e., $\mathbf{x} = [x, x] \in \mathbb{R}^3$, with $\mathbf{x} \in \mathbb{R}^2$ and $x \in \mathbb{R}$. The calligraphic letters (\mathcal{F} , \mathcal{K} etc.) are used to denote operators.

A. Moving Target Model

Let $\mathbf{x} = [x, \psi(\mathbf{x})] \in \mathbb{R}^3$ denote a location on the ground, where $\mathbf{x} \in \mathbb{R}^2$ and $\psi: \mathbb{R}^2 \rightarrow \mathbb{R}$ is a known, smooth function for the ground topography. As usual, we assume that the scattering takes place in a thin region near the surface. Therefore, the scene is represented by the two-dimensional reflectivity function $\rho: \mathbb{R}^2 \rightarrow \mathbb{R}$.

Let $\mathbf{v}_{\mathbf{x}} \in \mathbb{R}^2$ denote the 2-D velocity of a ground-moving target located at \mathbf{x} at some reference time. Then, its three-dimensional velocity is given by $\mathbf{v}_{\mathbf{x}} = [\mathbf{v}_{\mathbf{x}}, \nabla_{\mathbf{x}}\psi(\mathbf{x}) \cdot \mathbf{v}_{\mathbf{x}}]$ where $\nabla_{\mathbf{x}}\psi(\mathbf{x})$ is the gradient of $\psi(\mathbf{x})$. We refer to $\mathbf{v}_{\mathbf{x}}$ (or $\mathbf{v}_{\mathbf{x}}$) for all \mathbf{x} as the *velocity field* of the scene. We define a model for the velocity field as follows:

$$\mathbf{v}_{\mathbf{x}} = \sum_{i=1}^N \mathbf{v}_{\mathbf{x}_i} \varphi(\mathbf{x} - \mathbf{x}_i) \quad (1)$$

where $\varphi(\mathbf{x} - \mathbf{x}_i)$ is a smooth differentiable function that approximates Dirac-delta distribution $\delta(\mathbf{x} - \mathbf{x}_i)$ in the limit and N represents the number of distinct moving targets in the scene. An example for $\varphi(\mathbf{x} - \mathbf{x}_i)$ is $e^{-\frac{|\mathbf{x} - \mathbf{x}_i|^2}{\sigma_i}}$, $\sigma_i \ll 1$, where σ_i can be chosen based on the image resolution and the physical extend of targets. Note that for well-separated targets, as $\mathbf{x} \rightarrow \mathbf{x}_i$, so does $\mathbf{v}_{\mathbf{x}} \rightarrow \mathbf{v}_{\mathbf{x}_i}$.

B. Forward Model

Let s denote the *slow-time* parameter¹ and $\gamma_T(s)$, $\gamma_R(s) \in \mathbb{R}^3$, $s \in [s_0, s_1] \subseteq \mathbb{R}$ be the transmitter and receiver trajectories, respectively.

Let

$$R(s, \mathbf{x}) = |\mathbf{x} - \gamma_R(s)| + |\mathbf{x} - \gamma_T(s)| \quad (2)$$

be the *bistatic range* and $(\widehat{\mathbf{x} - \gamma_R(s)})$ and $(\widehat{\mathbf{x} - \gamma_T(s)})$ denote the unit vectors from the receiver/transmitter to the scatterer. Then,

$$\mathbf{L}(s, \mathbf{x}) = (\widehat{\mathbf{x} - \gamma_R(s)}) + (\widehat{\mathbf{x} - \gamma_T(s)}) \quad (3)$$

defines the three-dimensional (3D) *bistatic look-direction*.

¹In wide-band pulsed SAR, the slow-time parameter is associated with the pulse number or the processing interval [7].

We assume that the antennas are in the far-field of the scene and model the received signal, d , as follows [3], [7], [43]:

$$d(s, t) = \mathcal{F}[\rho](s, t) := \int e^{-i\phi_v(\omega, s, t, \mathbf{x})} A_v(\omega, s, \mathbf{x}) \rho(\mathbf{x}) d\mathbf{x} d\omega, \quad (4)$$

where t denotes the *fast-time* variable, c_0 is the speed of light in free-space and ω denotes the temporal frequency. The phase function, ϕ_v , is given by

$$\phi_v(\omega, s, t, \mathbf{x}) = \omega(t - [R(s, \mathbf{x}) + B(s, \mathbf{x}, \mathbf{v}_\mathbf{x})]/c_0), \quad (5)$$

$$B(s, \mathbf{x}, \mathbf{v}_\mathbf{x}) = \mathbf{L}(s, \mathbf{x}) \cdot \mathbf{v}_\mathbf{x} s^2 \quad (6)$$

The complex amplitude function, A_v , includes the transmitter and receiver antenna beam patterns, transmitted waveforms, geometrical spreading factors, etc. We assume that for some m_A , A_v satisfies

$$\sup_{(\omega, s, \mathbf{x}) \in U} \left| \partial_\omega^{\alpha_\omega} \partial_s^{\beta_s} \partial_{x_1}^{\epsilon_1} \partial_{x_2}^{\epsilon_2} A_v(\omega, s, \mathbf{x}) \right| \leq C_A (1 + \omega^2)^{(m_A - |\alpha_\omega|)/2} \quad (7)$$

where U is any compact subset of $\mathbb{R} \times \mathbb{R} \times \mathbb{R}^2$ and C_A depends on U , α_ω , β_s , ϵ_1 and ϵ_2 . Under this assumption, \mathcal{F} becomes a Fourier integral operator (FIO) [16], [44], [45]. We refer to \mathcal{F} in (4) as the *forward model* for the bistatic SAR moving target imaging. Note that $\mathbf{v}_\mathbf{x}$ is an unknown but a constant parameter in \mathcal{F} . Neither its phase function nor its amplitude is a function of $\mathbf{v}_\mathbf{x}$.

C. Backprojection-Based Image Formation

It can be shown that given the velocity of the targets, a focused reflectivity image of the scene can be formed by back-projection [43]. However, target velocities are rarely available a priori for motion compensation. An alternative approach is to assume a constant hypothetical velocity for the whole scene and reconstruct an image that is focused only for those targets whose velocities are equal to the hypothesized velocity. One can then form a stack of reflectivity images, each one corresponding to a constant velocity, for a range of hypothesized velocities and estimate the velocity of moving targets by choosing the focused reflectivity images from the stack.

Therefore, assuming a constant velocity \mathbf{v}_h for the entire scene, we form a reflectivity image of the scene with the following backprojection operator:

$$\begin{aligned} \hat{\rho}_{\mathbf{v}_h}(\mathbf{z}) &= \mathcal{K}_{\mathbf{v}_h}[d](\mathbf{z}), \\ &= \int e^{i\phi_v(\omega, s, t, \mathbf{z})} Q_{\mathbf{v}_h}(\omega, s, \mathbf{z}) d(s, t) dt ds d\omega, \end{aligned} \quad (8)$$

where $\hat{\rho}_{\mathbf{v}_h}(\mathbf{z})$ is the reconstructed image corresponding to the hypothetical velocity \mathbf{v}_h and $Q_{\mathbf{v}_h}$ is a filter that can be determined with respect to a variety of criterion [13], [46], [47]. We assume that $Q_{\mathbf{v}_h}$ satisfies an assumption similar to the one in (7). Under this assumption (8) defines $\mathcal{K}_{\mathbf{v}_h}$ as a FIO³.

²Note that B is the bistatic spatial displacement due to the movement of targets.

³Note that \mathbf{v}_h is not a parameter of $\mathcal{K}_{\mathbf{v}_h}$, it is simply a constant.

III. PROPAGATION OF VISIBLE EDGES FROM THE SCENE TO THE RECONSTRUCTED IMAGES

In images, edges contain significant information. Therefore, a good image formation method is expected to preserve the edges, in the sense that the location and orientation of the edges in reconstructed images should be the same as that of the scene or object that is imaged. In SAR images, an edge may be a point-like structure (for a ‘‘point target’’) or a curvilinear structure (for an ‘‘extended target’’). The visible edges of a scene are those edges whose location and orientation information is acquired by the imaging process, and hence, contained by the received signal. Microlocal analysis, a theory of FIOs and singularities, provides concepts and techniques to analyze the propagation of singularities/edges from a scene to the data and from the data to the reconstructed image [16], [44], [45]. In particular, the concept of wavefront set identifies the location and orientation of the edges and the concept of canonical relationship describes how the singularities/edges of the scene is propagated by a FIO into data [48]. The canonical relationship associated with \mathcal{F} is given by

$$\begin{aligned} \mathcal{C}_\mathcal{F} &= \{(s, t, \partial_{s,t}\phi_v; \mathbf{x}, -\partial_\mathbf{x}\phi_v) \\ &\text{such that } \partial_\omega\phi_v(\omega, s, t, \mathbf{x}) = 0\}. \end{aligned} \quad (9)$$

$\mathcal{C}_\mathcal{F}$ tells us that if there is an edge at \mathbf{x} with orientation $-\partial_\mathbf{x}\phi_v$, then it gets propagated to a singularity at s, t with orientation $\partial_{s,t}\phi_v$ in the data as long as \mathbf{x} and s, t satisfy the condition $\partial_\omega\phi_v(\omega, s, t, \mathbf{x}) = 0$.

Since both the forward map \mathcal{F} and the inverse map $\mathcal{K}_{\mathbf{v}_h}$ are FIOs, we can study how the image fidelity operator $\mathcal{K}_{\mathbf{v}_h}\mathcal{F}$ maps the visible edges of the scene to the reconstructed image by means of Hörmander-Sato lemma [48]. This lemma states that

$$WF(\mathcal{K}_{\mathbf{v}_h}\mathcal{F}) \subseteq \mathcal{C}_{\mathcal{K}_{\mathbf{v}_h}} \circ \mathcal{C}_\mathcal{F} \quad (10)$$

where $WF(\mathcal{K}_{\mathbf{v}_h}\mathcal{F})$ denotes the wavefront set of the kernel of $\mathcal{K}_{\mathbf{v}_h}\mathcal{F}$ and $\mathcal{C}_{\mathcal{K}_{\mathbf{v}_h}}$, $\mathcal{C}_\mathcal{F}$ denote the canonical relations of $\mathcal{K}_{\mathbf{v}_h}$ and \mathcal{F} , respectively. \circ stands for the composition of the canonical relationships [16], [48].

A visible edge of the scene located at \mathbf{x} with orientation $-\partial_\mathbf{x}\phi_v$ is reconstructed at location \mathbf{z} with orientation $-\partial_\mathbf{z}\phi_v$ in the backprojection image as long as \mathbf{x} and \mathbf{z} satisfy the following criticality conditions:

$$\begin{aligned} R(s, \mathbf{x}) + B(s, \mathbf{x}, \mathbf{v}_\mathbf{x}) &= R(s, \mathbf{z}) + B(s, \mathbf{z}, \mathbf{v}_h), \quad (11) \\ \partial_s R(s, \mathbf{x}) + \partial_s B(s, \mathbf{x}, \mathbf{v}_\mathbf{x}) &= \partial_s R(s, \mathbf{z}) + \partial_s B(s, \mathbf{z}, \mathbf{v}_h). \quad (12) \end{aligned}$$

(11) and (12) define iso-range and iso-Doppler contours respectively for a target at location \mathbf{x} . For both equations, the left-hand-side of the equality corresponds to the measured range and Doppler and the right-hand-side corresponds to the range and Doppler used in the image formation process.

(11) and (12) show that to obtain a focused SAR image of moving targets imaging parameters on the right-hand-side must match to the measured or actual quantities on the left-hand-side of (11) and (12). Specifically, for each scatterer located at \mathbf{x} , the velocity \mathbf{v}_h used in the image formation must be $\mathbf{v}_\mathbf{x}$, the actual

velocity of the scatterer at position \mathbf{x} . If so⁴, the solution of (11) and (12) becomes $\mathbf{x} = \mathbf{z}$, which means that the scatterer at \mathbf{x} is reconstructed at the right position. If, on the other hand, the velocity \mathbf{v}_h used in the image formation is incorrect, the solution of (11) and (12) becomes $\mathbf{x} \neq \mathbf{z}$, resulting in positioning errors.

IV. POSITION ERROR ANALYSIS DUE TO MOVING TARGETS IN BISTATIC SAR IMAGES

Suppose a target located at \mathbf{x} when $s = 0$ is moving with velocity \mathbf{v}_x . We assume that we use an erroneous hypothetical velocity $\mathbf{v}_h = \mathbf{v}_z + \epsilon \Delta \mathbf{v}_z$ in the backprojection stage, where $\epsilon \in \mathbb{R}$ is the error in the velocity \mathbf{v}_h and $\mathbf{v}_z = \mathbf{v}_x$. For the target imaged, the perturbation $\epsilon \Delta \mathbf{v}_z$ to the true velocity results in a shifted position $\mathbf{z}_\epsilon = \mathbf{z} + \Delta \mathbf{z}$ instead of the true position \mathbf{z} in the reconstructed image. Then, we have

$$R(s, \mathbf{x}) + B(s, \mathbf{x}, \mathbf{v}_x) = R(s, \mathbf{z} + \Delta \mathbf{z}) + B(s, \mathbf{z} + \Delta \mathbf{z}, \mathbf{v}_z + \epsilon \Delta \mathbf{v}_z), \quad (13)$$

$$\begin{aligned} \partial_s R(s, \mathbf{x}) + \partial_s B(s, \mathbf{x}, \mathbf{v}_x) \\ = \partial_s R(s, \mathbf{z} + \Delta \mathbf{z}) + \partial_s B(s, \mathbf{z} + \Delta \mathbf{z}, \mathbf{v}_z + \epsilon \Delta \mathbf{v}_z). \end{aligned} \quad (14)$$

(13) and (14) show that a scatterer at \mathbf{x} in the scene is mapped to a position at $\mathbf{z}_\epsilon = \mathbf{z} + \Delta \mathbf{z}$ in the reconstructed image at slow-time s .

We want to determine the first order approximation to the shift $\Delta \mathbf{z}$ due to the velocity error $\epsilon \Delta \mathbf{v}_z$. In order to determine $\Delta \mathbf{z}$, we assume $\epsilon \rightarrow 0$ and expand (13) and (14) in Taylor series around $\epsilon = 0$ and keep the first-order terms in ϵ . Then using Taylor series expansion on (13) and (14), we obtain

$$\begin{aligned} \epsilon \partial_\epsilon [R(s, \mathbf{z}) + B(s, \mathbf{z}, \mathbf{v}_z + \epsilon \Delta \mathbf{v}_z)]|_{\epsilon=0} \\ + \nabla_{\mathbf{z}} [R(s, \mathbf{z}) + B(s, \mathbf{z}, \mathbf{v}_z)] \cdot \Delta \mathbf{z} = 0, \end{aligned} \quad (15)$$

$$\begin{aligned} \epsilon \partial_\epsilon [\dot{R}(s, \mathbf{z}) + \dot{B}(s, \mathbf{z}, \mathbf{v}_z + \epsilon \Delta \mathbf{v}_z)]|_{\epsilon=0} \\ + \nabla_{\mathbf{z}} [\dot{R}(s, \mathbf{z}) + \dot{B}(s, \mathbf{z}, \mathbf{v}_z)] \cdot \Delta \mathbf{z} = 0, \end{aligned} \quad (16)$$

where $\dot{R} = \partial_s R$ and $\dot{B} = \partial_s B$.

In Appendix I, we show that (15) simplifies to the following relationship:

$$\boxed{\begin{aligned} \Delta \mathbf{z} \cdot D\psi(\mathbf{z})[\mathbf{L}(s, \mathbf{z}) - \mathbf{L}_v^\perp(s, \mathbf{z})] \\ = -\epsilon \Delta \mathbf{v}_z \cdot D\psi(\mathbf{z})\mathbf{L}(s, \mathbf{z}). \end{aligned}} \quad (17)$$

In (17), $D\psi(\mathbf{z})$ is an operator that projects three-dimensional vectors onto the tangent plane of the ground topography. Specifically, it is given by

$$D\psi(\mathbf{z}) = \begin{bmatrix} 1 & 0 & \partial_{z_1} \psi(\mathbf{z}) \\ 0 & 1 & \partial_{z_2} \psi(\mathbf{z}) \end{bmatrix} \text{ for } \mathbf{z} = [z_1, z_2]. \quad (18)$$

$\mathbf{L}(s, \mathbf{z})$ denotes the 3D bistatic look-direction, and $\mathbf{L}_v^\perp(s, \mathbf{z})$ involves vectors that are perpendicular to the transmitter and receiver look-directions. Specifically, it is the sum of the components of the target velocity along the directions perpendicular

to the transmitter and receiver look-directions normalized with the corresponding range terms. This vector is given by

$$\mathbf{L}_v^\perp(s, \mathbf{z}) = \left[\frac{\mathbf{v}_R^\perp s}{|\mathbf{z} - \gamma_R(s)|} + \frac{\mathbf{v}_T^\perp s}{|\mathbf{z} - \gamma_T(s)|} \right]. \quad (19)$$

The vectors \mathbf{v}_R^\perp and \mathbf{v}_T^\perp are the components of the three-dimensional velocities along the directions perpendicular to the look-directions of the receiver and transmitter, respectively. They are given explicitly as follows:

$$\mathbf{v}_R^\perp = (\mathbf{z} - \widehat{\gamma_R(s)})[(\mathbf{z} - \widehat{\gamma_R(s)}) \cdot \mathbf{v}_z] - \mathbf{v}_z, \quad (20)$$

$$\mathbf{v}_T^\perp = (\mathbf{z} - \widehat{\gamma_T(s)})[(\mathbf{z} - \widehat{\gamma_T(s)}) \cdot \mathbf{v}_z] - \mathbf{v}_z, \quad (21)$$

where $\hat{\mathbf{z}}$ denotes the unit vector in the direction of \mathbf{z} .

Similarly, (16) simplifies to the following relationship:

$$\boxed{\begin{aligned} \Delta \mathbf{z} \cdot D\psi(\mathbf{z})[\dot{\mathbf{L}}(s, \mathbf{z}) - \dot{\mathbf{L}}_v^\perp(s, \mathbf{z})] \\ = -\epsilon \Delta \mathbf{v}_z \cdot D\psi(\mathbf{z})[\mathbf{L}(s, \mathbf{z}) + \dot{\mathbf{L}}(s, \mathbf{z})s], \end{aligned}} \quad (22)$$

where $\dot{\mathbf{L}}(s, \mathbf{z})$ and $\dot{\mathbf{L}}_v^\perp(s, \mathbf{z})$ stand for the derivatives of $\mathbf{L}(s, \mathbf{z})$ and $\mathbf{L}_v^\perp(s, \mathbf{z})$, with respect to the slow-time variable s , respectively. These vectors are explicitly given as follows:

$$\dot{\mathbf{L}}(s, \mathbf{z}) = \left[\frac{\dot{\gamma}_R^\perp(s)}{|\mathbf{z} - \gamma_R(s)|} + \frac{\dot{\gamma}_T^\perp(s)}{|\mathbf{z} - \gamma_T(s)|} \right], \quad (23)$$

$$\begin{aligned} \dot{\mathbf{L}}_v^\perp(s, \mathbf{z}) = \\ \left[\frac{(\dot{\mathbf{v}}_R^\perp s + \mathbf{v}_R^\perp)|\mathbf{z} - \gamma_R(s)| + \mathbf{v}_R^\perp s[(\mathbf{z} - \widehat{\gamma_R(s)}) \cdot \dot{\gamma}_R(s)]}{|\mathbf{z} - \gamma_R(s)|^2} \right. \\ \left. + \frac{(\dot{\mathbf{v}}_T^\perp s + \mathbf{v}_T^\perp)|\mathbf{z} - \gamma_T(s)| + \mathbf{v}_T^\perp s[(\mathbf{z} - \widehat{\gamma_T(s)}) \cdot \dot{\gamma}_T(s)]}{|\mathbf{z} - \gamma_T(s)|^2} \right], \end{aligned} \quad (24)$$

where $\dot{\mathbf{v}}_R^\perp = \partial_s \mathbf{v}_R^\perp$, $\dot{\mathbf{v}}_T^\perp = \partial_s \mathbf{v}_T^\perp$, $\dot{\gamma}_R(s) = \partial_s \gamma_R(s)$ and $\dot{\gamma}_T(s) = \partial_s \gamma_T(s)$ are the three-dimensional receiver and transmitter antenna velocities. In (23), $\dot{\gamma}_R^\perp(s)$ and $\dot{\gamma}_T^\perp(s)$ are the components of the receiver and transmitter antenna velocities in the directions perpendicular to the look-directions of the receiver and transmitter, respectively. They are given as follows:

$$\dot{\gamma}_R^\perp(s) = (\mathbf{z} - \widehat{\gamma_R(s)})[(\mathbf{z} - \widehat{\gamma_R(s)}) \cdot \dot{\gamma}_R(s)] - \dot{\gamma}_R(s), \quad (25)$$

$$\dot{\gamma}_T^\perp(s) = (\mathbf{z} - \widehat{\gamma_T(s)})[(\mathbf{z} - \widehat{\gamma_T(s)}) \cdot \dot{\gamma}_T(s)] - \dot{\gamma}_T(s). \quad (26)$$

Note that $\dot{\mathbf{L}}(s, \mathbf{z})$ involves vectors that are orthogonal to the receiver and transmitter look-directions. However, $\dot{\mathbf{L}}(s, \mathbf{z})$ is not necessarily orthogonal to $\mathbf{L}(s, \mathbf{z})$. We refer to $\dot{\mathbf{L}}(s, \mathbf{z})$ as the three-dimensional *bistatic transverse look-direction*. Similarly, we refer to $\dot{\gamma}_R^\perp(s)$ and $\dot{\gamma}_T^\perp(s)$ as the *transverse receiver and transmitter velocities*, respectively.

Definitions: For ease of exposition, for the rest of the paper, we define the following terms and notation.

- 2D bistatic and transverse bistatic look-directions - Let

$$\mathbf{L}(s, \mathbf{z}) = D\psi(\mathbf{z})\mathbf{L}(s, \mathbf{z}), \quad (27)$$

$$\dot{\mathbf{L}}(s, \mathbf{z}) = D\psi(\mathbf{z})\dot{\mathbf{L}}(s, \mathbf{z}), \quad (28)$$

⁴under appropriate antenna trajectories and antenna illumination conditions

and $\widehat{\mathbf{L}}(s, \mathbf{z})$ and $\widehat{\dot{\mathbf{L}}}(s, \mathbf{z})$ represent the corresponding unit vectors. Since $\mathbf{L}(s, \mathbf{z})$ and $\dot{\mathbf{L}}(s, \mathbf{z})$ are the projections of the 3D bistatic and transverse look-directions onto the tangent plane of the ground topography, we refer to $\widehat{\mathbf{L}}(s, \mathbf{z})$ and $\widehat{\dot{\mathbf{L}}}(s, \mathbf{z})$ as the *2D bistatic look-direction* and *2D transverse bistatic look-direction*, respectively⁵.

- Components of the target positioning errors -

$$\text{Radial position error : } \Delta \mathbf{z}^r = \Delta \mathbf{z} \cdot \widehat{\mathbf{L}}(s, \mathbf{z}), \quad (29)$$

$$\text{Transverse position error : } \Delta \mathbf{z}^t = \Delta \mathbf{z} \cdot \widehat{\dot{\mathbf{L}}}(s, \mathbf{z}). \quad (30)$$

- Components of the target velocity -

$$\text{Radial target velocity : } \mathbf{v}_z^r = \mathbf{v}_z \cdot \widehat{\mathbf{L}}(s, \mathbf{z}), \quad (31)$$

$$\text{Transverse target velocity : } \mathbf{v}_z^t = \mathbf{v}_z \cdot \widehat{\dot{\mathbf{L}}}(s, \mathbf{z}). \quad (32)$$

Note that the components of the positioning error and target velocity as defined above are slow-time dependent. However, this dependency is dropped to simplify the notation.

In general, $\mathbf{L}(s, \mathbf{z})$ and $\dot{\mathbf{L}}(s, \mathbf{z})$ are not orthogonal to each other. However, for certain geometric configurations, these directions become orthogonal to each other. In particular, if the transmitter and receiver velocities are parallel and orthogonal to the transmitter and receiver look-directions, then $\mathbf{L}(s, \mathbf{z})$ and $\dot{\mathbf{L}}(s, \mathbf{z})$ become orthogonal to each other. Furthermore, if the antennas are flying at a constant height, 2D bistatic and transverse bistatic look-directions become orthogonal to each other. Clearly, these conditions are satisfied for a monostatic antenna flying at a constant height. When $\mathbf{L}(s, \mathbf{z})$ and $\dot{\mathbf{L}}(s, \mathbf{z})$ are orthogonal, the radial and transverse components of both the position error and target velocity become orthogonal.

Remarks: We now summarize the implications of (17) and (22).

- The position error analysis in (17) and (22) is applicable to both point and extended targets.
- Note that in both equations (17) and (22) \mathbf{z} denotes the correct location of the scatterer in the reconstructed image. The shift $\Delta \mathbf{z}$, or the positioning error, lies at the intersection of the solutions of (17) and (22).
- *Positioning error under stationary scene assumption:* If the image is reconstructed under the assumption that the scene is stationary [12], the positioning error in backprojection-based images is given by (17) and (22) with $\epsilon \Delta \mathbf{v}_z = -\mathbf{v}_z$ where \mathbf{v}_z is the true velocity of the target at $\mathbf{z} = \mathbf{x}$.
- *Positioning errors in bistatic and transverse look-directions:* (17) shows the component of the positioning error along the vector $D\psi(\mathbf{z})[\mathbf{L}(s, \mathbf{z}) - \mathbf{L}_v^\perp(s, \mathbf{z})]$ and (22) shows its components along the vector $D\psi(\mathbf{z})[\dot{\mathbf{L}}(s, \mathbf{z}) - \dot{\mathbf{L}}_v^\perp(s, \mathbf{z})]$. The positioning error in each direction is directly proportional to the component of the velocity \mathbf{v}_z along the vectors $D\psi(\mathbf{z})\mathbf{L}(s, \mathbf{z})$

⁵For the rest of the paper, we drop the terms 3D and 2D while referring to $\mathbf{L}(s, \mathbf{z})$, $\mathbf{L}(s, \mathbf{z})$, $\dot{\mathbf{L}}(s, \mathbf{z})$ and $\dot{\mathbf{L}}(s, \mathbf{z})$ unless the distinction is not clear from the context.

and $D\psi(\mathbf{z})[\mathbf{L}(s, \mathbf{z}) + \dot{\mathbf{L}}(s, \mathbf{z})s]$, respectively. In a typical imaging scenario, antenna ranges are much larger than the distances traveled by moving targets throughout the aperture. Additionally, the transmitting and receiving antennas move much faster than typical ground targets. Therefore, we approximate

$$\mathbf{L}(s, \mathbf{z}) - \mathbf{L}_v^\perp(s, \mathbf{z}) \approx \mathbf{L}(s, \mathbf{z}), \quad (33)$$

$$\dot{\mathbf{L}}(s, \mathbf{z}) - \dot{\mathbf{L}}_v^\perp(s, \mathbf{z}) \approx \dot{\mathbf{L}}(s, \mathbf{z}). \quad (34)$$

Under these approximations and using the notation introduced above, (17) and (22) become

$$\Delta \mathbf{z}^r = \mathbf{v}_z^r s, \quad (35a)$$

$$\Delta \mathbf{z}^t = \mathbf{v}_z^r \frac{2|D\psi(\mathbf{z})\widehat{\mathbf{L}}(s, \mathbf{z})| \cos(\Theta(s, \mathbf{z})/2)}{|\dot{\mathbf{L}}(s, \mathbf{z})|} + \mathbf{v}_z^t s. \quad (35b)$$

where $\Theta(s, \mathbf{z})$ is the *bistatic angle*, i.e., the angle between the receiver and transmitter look-directions, $(\mathbf{z} - \widehat{\gamma}_R(s))$ and $(\mathbf{z} - \widehat{\gamma}_T(s))$. When the ground topography is flat, the magnitude $|D\psi(\mathbf{z})\widehat{\mathbf{L}}(s, \mathbf{z})|$ equals to $\sin(\Phi(s, \mathbf{z}))$, where $\Phi(s, \mathbf{z})$ is the angle between $\widehat{\mathbf{L}}(s, \mathbf{z})$ and the normal vector of the ground plane.

- (35a) and (35b) describe the components of the positioning error in the bistatic look-direction and transverse bistatic look-direction in terms of the radial and transverse components of the target velocity located at \mathbf{z} . In general the components of the positioning error are not necessarily orthogonal, but in special configurations, as described above, they become orthogonal.
- (35a) shows that positioning error in the bistatic look-direction depends solely on the velocity of the target in the bistatic look-direction. (35b) shows that positioning errors in the transverse direction depends both on the radial and transverse components of the target velocity as well as the 3D bistatic angle and the transverse components of the transmitter and receiver velocities and the range of the antennas. Additionally, it shows that radial target velocity is the major contributor of the transverse positioning errors since $|\dot{\mathbf{L}}(s, \mathbf{z})|$ is inversely proportional to antenna ranges.
- The \mathbf{z} dependency of (35a) and (35b) accounts for the space dependent nature of the positioning error and s dependency of (35a) and (35b) explains the smearing due to moving targets observed in reconstructed images.
- *Positioning errors for short apertures and a small scene:* We assume that the receiver and transmitter traverse a short aperture such that the subtending angle covering the aperture is no more than a few degrees⁶. In this case,

⁶In typical imaging scenarios the subtending angle is no more than 7–10° to avoid “wide aperture” issues. Therefore, the “short aperture” assumptions is valid for most scenarios.

TABLE I

POSITIONING ERRORS WHEN THE TARGET VELOCITY \mathbf{v}_z IS ALONG THE BISTATIC OR TRANSVERSE BISTATIC LOOK-DIRECTIONS FOR A SHORT APERTURE AND A SMALL SCENE

Direction of target velocity	Radial position error	Transverse position error
Parallel to $\hat{\mathbf{L}}$	$\mathbf{v}_z s$	$\mathbf{v}_z 2 D\psi(\mathbf{z})\mathbf{L} \cos(\Theta/2)/ \hat{\mathbf{L}} $
Parallel to $\hat{\mathbf{L}}^\perp$	None	$\mathbf{v}_z s$

we can assume that $\hat{\mathbf{L}}(s, \mathbf{z})$, $\hat{\mathbf{L}}^\perp(s, \mathbf{z})$ can be replaced by slow-time independent directions $\hat{\mathbf{L}}$, $\hat{\mathbf{L}}^\perp$ and analyze (35a) and (35b) when the target velocity is parallel to 1) the bistatic look-direction $\hat{\mathbf{L}}$, and 2) the transverse bistatic look-direction $\hat{\mathbf{L}}^\perp$. (35a) shows that when the target is moving along the bistatic look-direction, the positioning error in the bistatic look-direction is proportional to the target velocity scaled by the slow-time variable s . This means that the target position is propagated to a different position for each s causing a ‘‘smearing’’ artifact. (35b) shows that the positioning error in the transverse bistatic look-direction is proportional to target velocity scaled by $2|D\psi(\mathbf{z})\mathbf{L}| \cos(\Theta/2)/|\hat{\mathbf{L}}|$. Since $|\hat{\mathbf{L}}|$ is inversely proportional to the reciprocal of the range of the antennas, the transverse positioning error dominates the radial positioning error. Furthermore, since the bistatic angle and the range of the antennas remain almost constant for a short aperture, smearing can be neglected. In this case, the target is simply displaced and focused at the wrong location. If the target velocity is parallel to the transverse bistatic look-direction, on the other hand, there is no positioning error along the bistatic look-direction and the one along the transverse direction is a smearing artifact proportional to the velocity of the target. These results are summarized in Table I.

V. POSITION ERRORS IN SPECIFIC GEOMETRIES FOR BISTATIC CONFIGURATIONS

In the following subsections, we analyze the moving target artifacts in backprojection images in commonly used SAR imaging geometries. Specifically, we consider the following cases: (1) a stationary transmitter and a moving antenna traversing a straight, linear trajectory at a constant height (see Fig. 1); (2) moving transmitter and receiver that are separated by a constant offset, each one traversing a linear trajectory at a constant height (see Fig. 2); In all of these cases, we assume a flat topography and a specific coordinate system and express (35a) and (35b) in terms of antenna velocities, bistatic and elevation angles and other configuration specific factors.

1) *Bistatic Configuration with a Stationary Transmitter*: We consider a stationary transmitter located at \mathbf{T} and a receiver traversing a trajectory $\gamma_R(s)$ at constant height h , with a velocity of $\dot{\gamma}_R(s) = [\mathbf{v}_a, 0]$ as shown in Fig. 1. Let $\Theta(s, \mathbf{z})$ be the bistatic angle and let $\Phi(s, \mathbf{z})$ be the *bistatic elevation angle*,

⁷We suppress the \mathbf{z} dependence of the look-directions to simplify our notation.

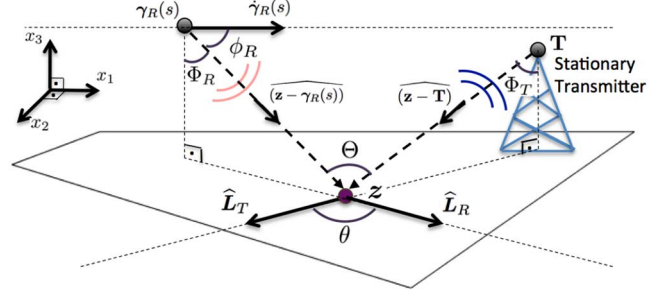


Fig. 1. Bistatic SAR acquisition geometry with a stationary transmitter located at \mathbf{T} and a moving receiver traversing the trajectory $\gamma_R(s)$ at a constant height h with a velocity of $[\mathbf{v}_a, 0]$. $\hat{\mathbf{L}}_T$ and $\hat{\mathbf{L}}_R$ are the 2D projections of the 3D transmitter and receiver look-directions $(\mathbf{z} - \mathbf{T})$ and $(\mathbf{z} - \gamma_R(s))$ onto the flat ground, respectively. $\phi_{R,T}$ is the angle between $(\mathbf{z} - \gamma_{R,T}(s))$ and $\hat{\gamma}_{R,T}(s)$. $\Phi_{R,T}$ is the elevation angle of the receiver/transmitter, i.e. angle between $(\mathbf{z} - \gamma_{R,T}(s))$ and the normal vector of the flat ground plane. Θ is the bistatic angle, i.e., the angle between $(\mathbf{z} - \mathbf{T})$ and $(\mathbf{z} - \gamma_R(s))$.

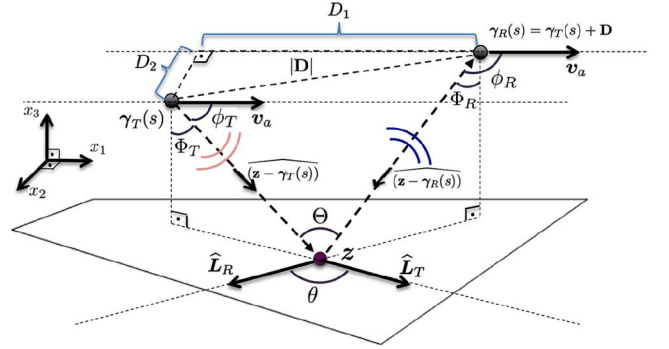


Fig. 2. Bistatic SAR acquisition geometry for a transmitter traversing $\gamma_T(s)$ at a constant height and a receiver traversing $\gamma_R(s) = \gamma_T(s) + \mathbf{D}$ with a constant offset $\mathbf{D} = [D_1, D_2, 0]$. The transmitter/receiver antenna velocity is $[\mathbf{v}_a, 0]$. $\hat{\mathbf{L}}_T$ and $\hat{\mathbf{L}}_R$ denote the projections of $(\mathbf{z} - \gamma_T(s))$ and $(\mathbf{z} - \gamma_R(s))$ onto the flat ground, respectively. $\phi_{T,R}$ is the angle between the transmitter/receiver look-direction and $[\mathbf{v}_a, 0]$. $\Phi_{T,R}$ is the transmitter/receiver elevation angle, i.e., the angle between the transmitter/receiver look-direction and the normal of the ground plane. Θ is the bistatic angle.

i.e., the angle between $\mathbf{L}(s, \mathbf{z})$ and the normal vector of the flat ground. Let $\Phi_R(s, \mathbf{z})$ be the elevation angle of the receiver, i.e., the angle between the normal of the ground plane and the receiver look-direction and $\phi_R(s, \mathbf{z})$ be the angle between the receiver look-direction and the velocity of the antenna. We can then re-express (35a) and (35b) as follows:

$$\Delta z^r = \mathbf{v}_z^r s, \quad (36)$$

$$\Delta z^t = \mathbf{v}_z^t \frac{2|\mathbf{z} - \gamma_R(s)| \sin(\Phi(s, \mathbf{z})) \cos(\Theta(s, \mathbf{z})/2)}{|\mathbf{v}_a| |\beta_R(s, \mathbf{z})|} + \mathbf{v}_z^t s. \quad (37)$$

where

$$\beta_R^2(s, \mathbf{z}) = \sin^2(\phi_R(s, \mathbf{z})) - \cos^2(\phi_R(s, \mathbf{z})) \cos^2(\Phi_R(s, \mathbf{z})). \quad (38)$$

See Appendix II for the derivation of (37). Note that for a short aperture, when the illuminated scatterers are in the

bore-sight direction of the receiver, β_R becomes ≈ 1 . We can then approximate (37) as follows:

$$\Delta z^t \approx \mathbf{v}_z^r \frac{2|\mathbf{z} - \gamma_R(s)| \sin(\Phi(s, \mathbf{z})) \cos(\Theta(s, \mathbf{z})/2)}{|\mathbf{v}_a|} + \mathbf{v}_z^t s. \quad (39)$$

From (37), we observe that if the target has a radial velocity component, the displacement in the transverse look-direction is directly proportional with the receiver antenna range and the bistatic elevation angle Φ . It is inversely proportional with the antenna speed $|\mathbf{v}_a|$, the bistatic angle Θ and β_R . The larger the bistatic angle and the antenna speed, the smaller the displacement becomes. The quantity β_R is determined by the receiver azimuthal and elevation angles, ϕ_R and Φ_R . The larger the azimuthal angle, the smaller β_R becomes, and hence, the larger the displacement is. On the other hand, irrespective of the receiver elevation angle, the larger the azimuthal angle ϕ_R , the larger β_R becomes, and hence, the smaller the displacement is.

Since the typical antenna ranges are much larger than the distances traveled by typical ground targets within one synthetic aperture, the positioning error in the transverse look-direction is dominated by the factors scaling the radial target velocity, not by the transverse target velocity. If, on the other hand, the target is traveling parallel to the antenna trajectory, the moving target induces a smearing artifact in the image along the antenna trajectory as shown by (36).

Note that for a receiver traversing a short aperture at a constant velocity far from a small scene, we can assume that the range of the receiver to the scene, and the angles $\Theta(s, \mathbf{z})$, $\Phi(s, \mathbf{z})$, $\Phi_R(s, \mathbf{z})$ and $\phi_R(s, \mathbf{z})$ remain approximately constant throughout the aperture.

2) *Bistatic Configuration with a Constant Offset between the Transmitter and Receiver:* We assume that the transmitter and receiver move in tandem along a short linear trajectory, at a constant velocity, separated with a constant offset vector \mathbf{D} as shown in Fig. 2. Let $\gamma_T(s)$ be the transmitter trajectory and $\gamma_R(s) = \gamma_T(s) + \mathbf{D}$ denote the receiver trajectory. Let $\dot{\gamma}_T(s) = \dot{\gamma}_R(s) = [\mathbf{v}_a, 0]$ be the velocity of the antennas. For a short linear aperture and a small scene, we assume that the bistatic angle Θ , and the bistatic elevation angle, Φ , remain constant throughout the aperture. Furthermore, we assume that the range of the transmitter and receiver measured with respect to the scene center are approximately equal and constant. Under these assumptions, we approximate $|D\psi(\mathbf{z})\hat{\mathbf{L}}(s, \mathbf{z})| \approx \sin(\Phi)$ and

$$D\psi(\mathbf{z})\hat{\mathbf{L}}(s, \mathbf{z}) \approx -\frac{2|\mathbf{v}_a| \sin(\Theta)\hat{\mathbf{v}}_a}{|\mathbf{D}|}. \quad (40)$$

See Appendix III for the derivation of (40). Plugging these approximations into (35b), we obtain

$$\Delta z^r = \mathbf{v}_z^r s, \quad (41)$$

$$\Delta z^t \approx \mathbf{v}_z^r \frac{|\mathbf{D}| \sin(\Phi) \cos(\Theta/2)}{|\mathbf{v}_a| \sin(\Theta)} + \mathbf{v}_z^t s, \quad (42)$$

where we drop the s and \mathbf{z} dependency in Θ and Φ . Note that from (23) and (35b), we know that Δz^t is directly proportional

to the ranges of the antennas and inversely proportional with the speed of the antennas in the transverse direction of the receiver and transmitter. However, for a short linear aperture and a small bistatic angle, the ranges of the antennas can be approximated by $|\mathbf{D}|/\sin(\Theta)$. Furthermore, in this particular configuration, the transverse bistatic look-direction $\hat{\mathbf{L}}$ is approximately in the direction of $-\hat{\mathbf{v}}_a$.

Similar to the results in Section V-1, if the target is moving parallel to the antennas, the backprojection images has smearing artifacts only in the transverse direction. If, on the other hand, the target is moving in the radial direction, the images have both the radial and transverse positioning errors. (42) shows that the positioning error in the transverse look-direction is inversely proportional to the speed of the antennas and the bistatic angle, Θ . It is directly proportional to $|\mathbf{D}|$, the distance between the antennas and the bistatic elevation angle, Φ .

VI. NUMERICAL SIMULATIONS

In this section, we present numerical simulations to verify our analysis. We study the positioning errors with respect to the length of the synthetic aperture, the direction of the target velocity with respect to antenna look-directions, the bistatic angle, the elevation angle, the antenna and target speeds, and the trajectory shape.

We consider the following bistatic configurations to validate our analysis: (1) a short linear aperture; (2) a wide linear aperture; (3) a wide circular aperture; and (4) a long aperture and a maneuvering target. In all four scenarios, without loss of generality we consider a point target moving at a constant velocity except the last case where we consider a maneuvering target. In each of these scenarios, we show that the moving target morphology in reconstructed images are consistent with the morphology predicted by our analysis. In addition to the visual comparison, we also compare the quantitative position errors predicted by our analysis with the position errors measured from reconstructed images. The analytical position errors are obtained using (41) and (42) for the short aperture case, and (35a) and (35b) for the wide aperture case. The measured position error is obtained from the reconstructed images by estimating the position of the target. The estimation is based on the brightest pixel and subaperture processing whereby the received data are divided into overlapping windows in slow-time and the target location is estimated for each slow-time. The backprojection filter Q_{v_n} is weighted with the slow-time s . This provides the artifacts to be stronger in intensity as the aperture time increases. Therefore, the brightest point in the reconstructed images corresponds to the end of the artifacts which we quantify with positioning error equations. We also note that our analysis is based on only the backprojection step and is valid for any type of filter. We demonstrate the effect of bistatic angle on the moving target morphologies in Scenario 1.

For all the simulations, the transmitted waveform has a bandwidth of 214 MHz with a carrier frequency of 10 GHz. The received signal is generated using (4). The images are reconstructed using the filtered-backprojection inversion given by (8) under the assumption that the scene is stationary. All of the reconstructed images are shown in dB scale.

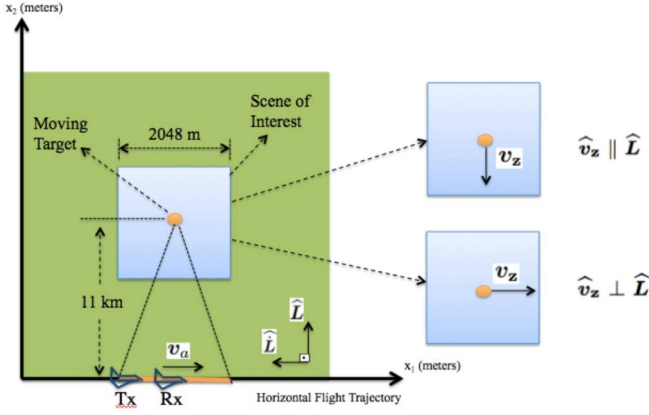


Fig. 3. An illustration of the simulation setup for the bistatic constant offset configuration. The bistatic look-direction \hat{L} is parallel to x_2 axis; and the transverse bistatic look-direction \hat{L} is parallel to x_1 axis. Two different directions for the target velocity, \mathbf{v}_z , are considered: i) \mathbf{v}_z is parallel to \hat{L} , ii) \mathbf{v}_z is parallel to \hat{L} .

For all the simulations, the scene is a flat plane centered at $[11, 11, 0]$ km. The size of the scene is $2048 \times 2048 \text{ m}^2$ for the short aperture simulations and $512 \times 512 \text{ m}^2$ for the long aperture simulations. The scene is discretized into 512×512 pixels. A point target with unit reflectivity moving with velocity \mathbf{v}_z is placed in the scene. Fig. 3 illustrates the coordinate system and the scene used for the simulations.

A. Scenario 1 - Bistatic Constant Offset Configuration with a Linear Short Aperture

We assume a short linear trajectory for the transmitter and receiver along x_1 axis as shown in Fig. 3. Both antennas are located at a height of 6.5 km moving with velocity of $\mathbf{v}_a = [70, 0] \text{ m/sec}$ (250 km/hr). The transmitter and receiver trajectories are given by $\gamma_T(s) = [10.31e3 + 70s, 0, 6.5e3] \text{ m}$ and $\gamma_R(s) = [11.69e3 + 70s, 0, 6.5e3] \text{ m}$, $s \in [0, 9.9] \text{ sec}$. Hence, the antennas are separated by a constant offset of $[1375, 0, 0] \text{ m}$. This corresponds to a bistatic angle Θ of approximately 6.2° . The aperture time is approximately 9.9 seconds, sampled uniformly at 4096 points. The total distance covered by the antennas during the aperture is 688 m. This leads to a subtending angle of 3.58° for the bistatic aperture. For this configuration, the bistatic look-direction \hat{L} is assumed to be approximately constant throughout the aperture; and the transverse bistatic look-direction \hat{L} is parallel to the antenna velocity \mathbf{v}_a and perpendicular to \hat{L} .

We assume two different directions for the point target velocity \mathbf{v}_z : i) $\mathbf{v}_z = \mathbf{v}_z^r = [0, -15, 0] \text{ km/hr}$ parallel to the x_2 axis, hence parallel to the bistatic look-direction \hat{L} ; ii) $\mathbf{v}_z = \mathbf{v}_z^t = [15, 0, 0] \text{ km/hr}$ parallel to the x_1 axis or the transverse bistatic look-direction \hat{L} .

1) *A Point Target Moving along the Bistatic Direction:* Fig. 4 shows the reconstructed images for different aperture lengths (“s” values), the last one corresponding to the full aperture image. The images in the boxes show the enlarged regions around the small areas indicated by the arrows. The solid and blank circles indicate the true (initial) and reconstructed

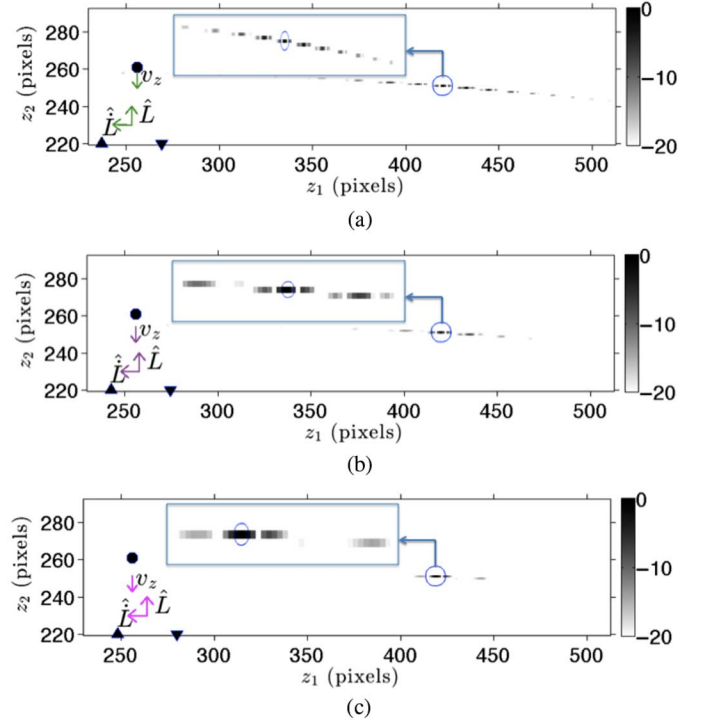


Fig. 4. The reflectivity images reconstructed for different aperture lengths Δs for a target moving along the bistatic direction and speed $v_z^t = |\mathbf{v}_z| = 15 \text{ km/hr}$. The bistatic SAR antennas are traversing a short horizontal trajectory at the same height and velocity with the bistatic angle of $\Theta = 6.2^\circ$. The artifacts are highlighted in zoomed images. The solid circle shows the true (initial) location of the target and the blank circle indicates the reconstructed position of the target based on the brightest spot. The arrows show the directions of \hat{L} , \hat{L} and \mathbf{v}_z . The up and down pointing triangles show the transmitter and receiver locations, respectively. (a) Reconstructed image ($\Delta s = 3.09 \text{ sec}$). (b) Reconstructed image ($\Delta s = 6.5 \text{ sec}$). (c) Reconstructed image ($\Delta s = 9.9 \text{ sec}$).

target locations, respectively. The reconstructed target is located (corresponds to the brightest pixel) along the transverse look-direction. This is due to the large range factor as predicted by (42). The smearing along the look-direction predicted by (41) is difficult to observe visually since it is very small as compared to the displacement along the transverse direction. The artifacts around the highest intensity pixel along the transverse direction are due limited aperture. These artifacts diminish as the aperture length (Δs) increases.

Figures 6(a) and 6(b) show the two components of the measured position errors (solid line) in the bistatic and transverse bistatic look-directions and compare these measured results to the analytic position errors (dashed line) computed from (41) and (42). We see that the transverse position error is larger than the radial position error. In the transverse look-direction the errors appear as large displacement since \mathbf{v}_z^r is scaled by large range factors as shown in (42). Along the bistatic look-direction, the displacement is s -dependent as shown by (41) and manifests as a smearing in the order of $\mathbf{v}_z s$. However, this smearing is very small as compared to the large displacements in the transverse look-direction making it difficult to make accurate estimation due to drastically different scales. Hence, in this case, the reconstructed image appears focused at a displaced location.

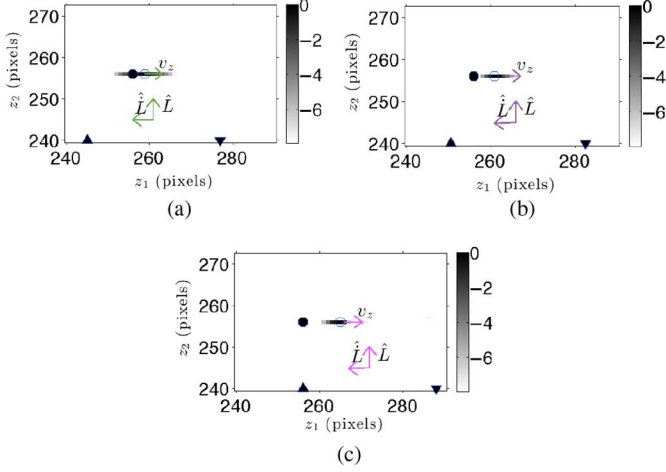


Fig. 5. The reflectivity images reconstructed for different aperture lengths Δs for a target moving horizontally with $|\mathbf{v}_z| = 15$ km/hr. The bistatic SAR antennas are traversing a short horizontal trajectory at the same height and velocity with the bistatic angle $\Theta = 6.2^\circ$. The solid circle shows the true (initial) location of the target. The blank circle indicates the reconstructed position of the target. Arrows show the directions of $\hat{\mathbf{L}}$, $\hat{\mathbf{L}}$ and \mathbf{v}_z . The up and down pointing triangles show the transmitter and receiver locations, respectively. (a) Reconstructed image ($\Delta s = 3.09$ sec). (b) Reconstructed image ($\Delta s = 6.50$ sec). (c) Reconstructed image ($\Delta s = 9.90$ sec).

2) *A Point Target Moving along the Transverse Bistatic Direction:* Fig. 5 shows the reconstructed images when the target is moving along the transverse bistatic look-direction with $|\mathbf{v}_z| = 15$ km/h. The solid and blank circles indicate the true (initial) and reconstructed target locations, respectively. The reconstructed images show smearing along the transverse look-direction proportional to $\mathbf{v}_z s$ as predicted by (41). There are no visible artifacts along the look-direction as predicted by (42). However, we observe some limited-aperture artifacts along the azimuthal direction especially for small Δs .

Figures 6(c) and 6(d) show the two components of the measured position errors (solid line) in the bistatic and transverse bistatic look-directions and compare these to the analytic position errors (dashed line) computed from (41) and (42). As expected, the measured errors in the look-direction is zero, whereas the measured error in the transverse look-direction is linearly increasing with the slow-time s consistent with (41) and (42).

3) *Moving Target Positioning Errors and Bistatic Angle:* For the imaging configuration depicted in Fig. 3, we fix the target velocity at $|\mathbf{v}_z| = 15$ km/hr and gradually increase the bistatic angle Θ from 0° (i.e. monostatic configuration) to 25° to compare the measured position errors with the ones predicted by (41) and (42). All analytic and measured displacements are computed for the full-aperture (i.e., the largest s value) images. The results are shown in Fig. 7. As Θ increases, the radial positioning errors remain constant when $\hat{\mathbf{v}}_z \perp \hat{\mathbf{L}}$ as shown in Figures 7(c) and 7(d), since these errors are Θ independent. The same result can be also observed for the radial positioning error when $\hat{\mathbf{v}}_z \parallel \hat{\mathbf{L}}$ as illustrated in Fig. 7(a). The only direction in which the position error is Θ dependent is the transverse bistatic look-direction displacement when $\hat{\mathbf{v}}_z \parallel \hat{\mathbf{L}}$. The error in this direction increases with Θ as shown by the analytic and measured error plots in Fig. 7(b).

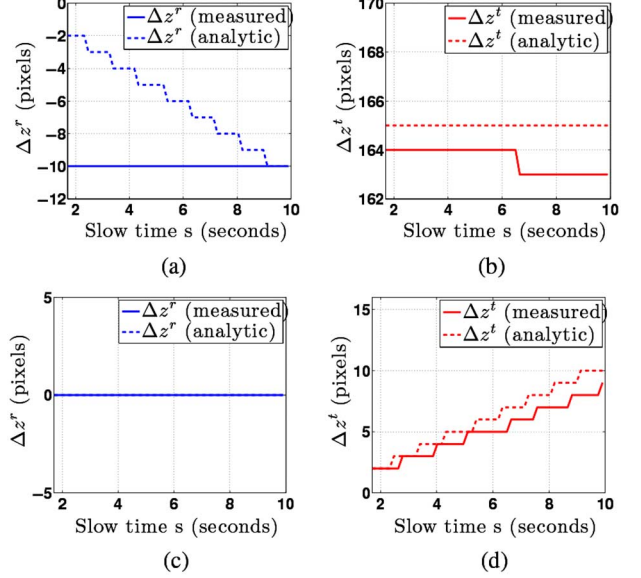


Fig. 6. The measured (solid) and analytic (dashed) position errors (in pixels) along the radial (i.e. Δz^r direction, shown on the left side) and transverse (i.e. Δz^t , shown on the right side) bistatic look-directions for increasing slow-time. The target is moving with a speed of $|\mathbf{v}_z| = 15$ km/hr in a), b) the bistatic direction (6(a),6(b)) and c), d) the transverse bistatic direction. The bistatic angle is $\Theta = 6.2^\circ$.

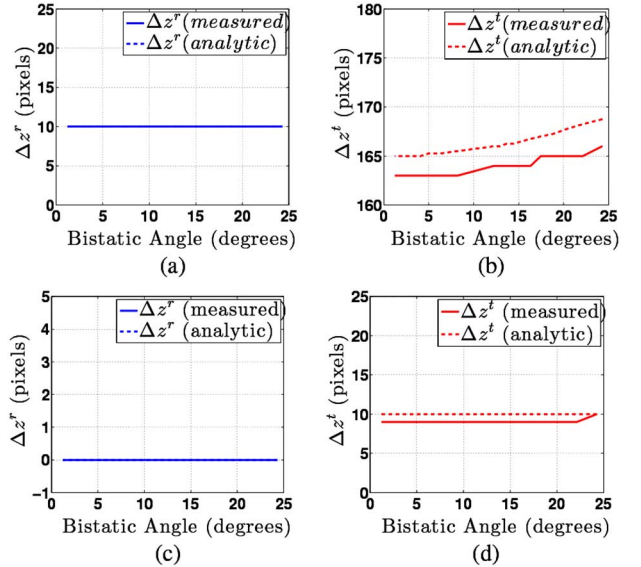


Fig. 7. The measured (solid) and analytic (dashed) position errors (in pixels) along the bistatic (7(a), 7(c)) and transverse bistatic look-directions (7(b), 7(d)) versus the bistatic angle Θ . The target is moving with the velocity $|\mathbf{v}_z| = 15$ km/hr in i) the bistatic direction, i.e. $\hat{\mathbf{v}}_z = \mathbf{v}_z$ (7(a), 7(b)) and ii) the transverse bistatic direction, i.e. $\hat{\mathbf{v}}_z = \mathbf{v}_z$ (7(c), 7(d)).

Note that similar images and position error results can be obtained for the bistatic configuration involving a stationary transmitter. However, for this case, the displacement error along the transverse look-direction is larger than that of the previous case, since this error is proportional to the large receiver range instead of the term $|\mathbf{D}|/\sin(\Theta)$ involved in the previous case.

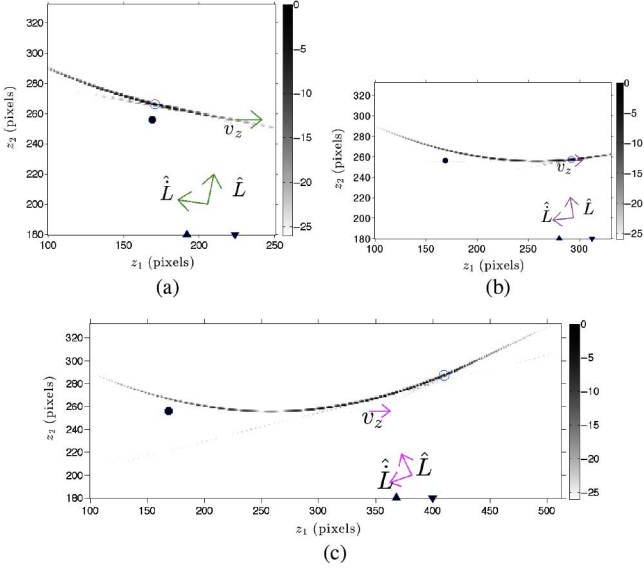


Fig. 8. The reflectivity images reconstructed for different aperture lengths Δs for a target with horizontal motion ($|v_z| = 4$ km/hr). The bistatic SAR antennas are traversing a long horizontal trajectory at the same height and velocity with the bistatic angle Θ varying between 5.3° to 6.2° . The solid circle shows the true (initial) location and the blank circle shows the reconstructed position of the target. The arrows show the directions of \hat{L} , \hat{L} and v_z . The up and down pointing triangles show the transmitter and receiver locations, respectively. (a) Reconstructed image ($\Delta s = 49.50$ sec). (b) Reconstructed image ($\Delta s = 103.95$ sec). (c) Reconstructed image ($\Delta s = 158.40$ sec).

B. Scenario 2 - Bistatic Constant Offset Configuration with a Linear Wide Aperture

We assume a long trajectory for the transmitter and receiver along x_1 axis as shown in Fig. 3. Both antennas are located at the same height, traveling at the same velocity with a constant distance apart as in the case of the short-aperture simulations. The antenna trajectories are $\gamma_T(s) = [4.81e3 + 70s, 0, 6.5e3]$ m and $\gamma_R(s) = [6.19e3 + 70s, 0, 6.5e3]$ m, $s \in [0, 158.4]$ sec. The aperture time is approximately 168 seconds, sampled uniformly at 4096 points. Due to the long aperture, the bistatic angle Θ varies between 5.3° and 6.2° . The total distance covered by the antennas during the aperture is 10.3 km. This leads to a subtending angle of 44° for the bistatic aperture.

For this configuration, the bistatic look-direction \hat{L} and the transverse bistatic look-direction \hat{L} vary throughout the aperture. We assume a point target traveling along x_1 axis with $|v_z| = 4$ km/hr. Figure 8 shows the reconstructed images for three different aperture lengths, the last one corresponding to the full aperture image. The images include the directions of \hat{L} , \hat{L} at the end of the aperture, initial and reconstructed positions of the target and the target velocity directions. At the beginning and end of the aperture, the component of the velocity projected onto the look-direction is at its highest value. During the aperture this component slowly decreases, at the midpoint of the aperture it becomes zero, and then starts to increase again. This component causes the displacement of the target along the transverse look-direction as shown in the first and third image and as predicted by (35b). The smearing observed along the transverse look-direction is due to the component of the target

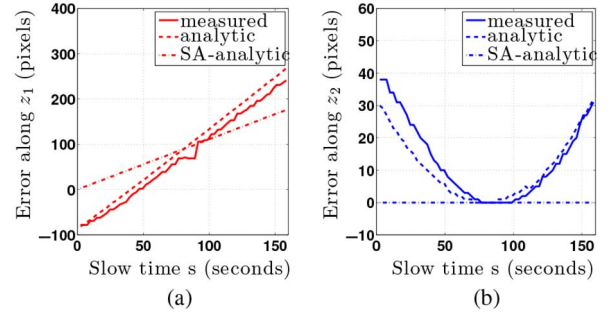


Fig. 9. The measured position errors (solid) and long-aperture analytic position errors (dashed - calculated from (35a) and (35b)) and short-aperture analytic position errors (SA-analytic shown in point-dashed - calculated from (41) and (42)) along x_1 and x_2 directions for increasing aperture length, slow-time. The target is moving along x_1 (horizontal) direction with $|v_z| = 4$ km/hr.

velocity along the transverse look-direction. The combination of these two positioning errors results in a concave parabola shaped artifact in the final reconstructed image.

Fig. 9 shows the two components of the measured position error (solid line) and analytic position errors (dashed line) in z_1 and z_2 directions. The analytic position errors are computed from equations (35a) and (35b). Fig. 9 also shows the analytic position errors under the short aperture assumptions calculated from equations (41) and (42). We see that the measured errors follow our theoretical result given by equations (35a) and (35b), but deviate from the analytical errors provided by equations (41) and (42). This is because the results in (35a) and (35b) are applicable for arbitrary imaging geometries including wide apertures, whereas (41) and (42) are only applicable to short linear apertures.

C. Scenario 3 - Bistatic Constant Offset Configuration with a Circular Wide Aperture

We consider a circular trajectory of 11 km radius. The transmitter trajectory is $\gamma_T(s) = [11e3 + 11e3 \cos(2\pi 70s), 11e3 + 11e3 \sin(2\pi 70s), 6.5e3]$ m, $s \in [0, 995.26]$ sec. The receiver trajectory follows the same circular trajectory with a constant angular offset such that the bistatic angle is about 6.12° throughout the aperture. The aperture time is approximately 995 seconds, sampled uniformly at 4096 points. Other imaging parameters are the same as in the previous scenarios. A point target is placed in the scene moving along x_1 axis with velocity $v_z = [0.75, 0]$ km/hr.

Fig. 10 shows the reconstructed images for different aperture lengths. The curved moving target morphology is induced by the rotating bistatic look-direction with respect to the fixed target velocity direction. We see in Fig. 10(a) that as the antennas rotate in the counter clockwise direction along the circle, the transverse component of the target velocity reduces and the radial component increases. This results in a displacement along z_2 direction, while smearing diminishes. In Fig. 10(b), as the antennas traverse along the second quarter, the transverse velocity component increases resulting in positioning of the target along z_1 direction. The same cycle repeats for Figures 10(c) and 10(d), resulting in a final moving target morphology resembling to four quarter circles at the end of the

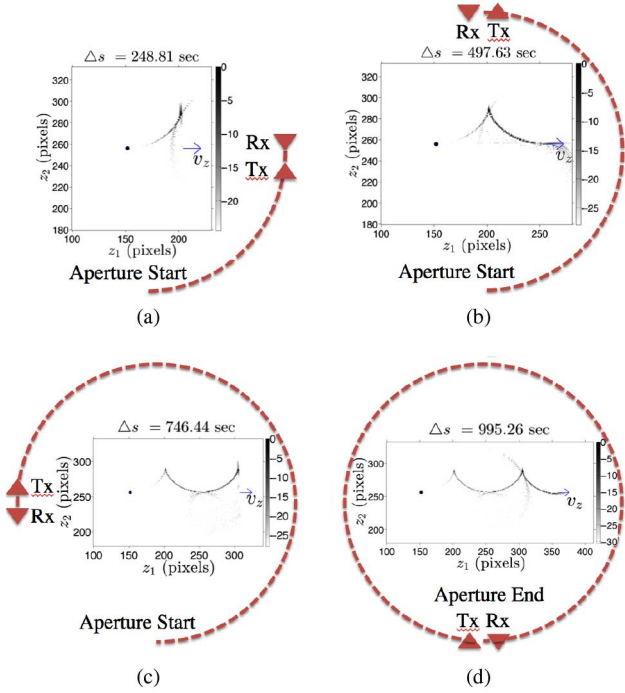


Fig. 10. The reflectivity images reconstructed for different aperture lengths. The bistatic SAR antennas are traversing a circular trajectory at a constant height and fixed velocity with the bistatic angle of $\Theta = 6.2^\circ$. A target is moving horizontally with $|v_z| = 0.75$ km/hr. The red circle shows the true (initial) location of the target. The arrows show the target location and motion. The dashed curve shows the trajectory of the antennas with the antenna positions shown by up and down pointing triangles for some slow-times. (a) Reconstructed image ($\Delta s = 248.81$ sec). (b) Reconstructed image ($\Delta s = 497.63$ sec). (c) Reconstructed image ($\Delta s = 746.44$ sec). (d) Reconstructed image ($\Delta s = 995.26$ sec).

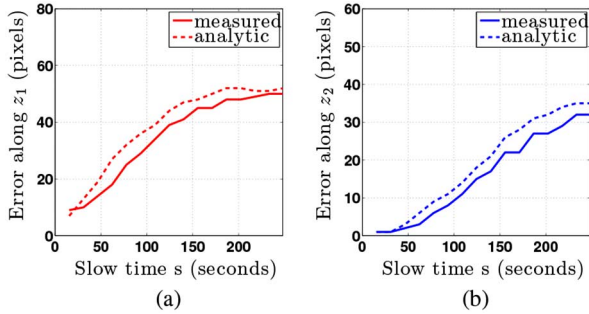


Fig. 11. The measured position errors (solid) and long-aperture analytic position errors (dashed - calculated from (35a) and (35b)) along x_1 and x_2 directions for increasing aperture length, slow-time until $\Delta s = 248.81$ sec. The target is moving along x_1 (horizontal) direction with $|v_z| = 0.75$ km/hr.

aperture. Fig. 11 shows the measured and analytic position errors for the first quarter of the trajectory, i.e. until $\Delta s = 248.81$ sec. (The errors for the following three quarters of the aperture are not shown since they are similar to those of the first quarter of the aperture.) Clearly, the measured errors are in agreement with the analytic errors predicted by (35a) and (35b).

D. Scenario 4 - Bistatic Constant Offset Linear Wide Aperture with a Maneuvering Target

We consider the same bistatic configuration as in Scenario 2, but with a maneuvering target. Figures 12(a) and (b) show the

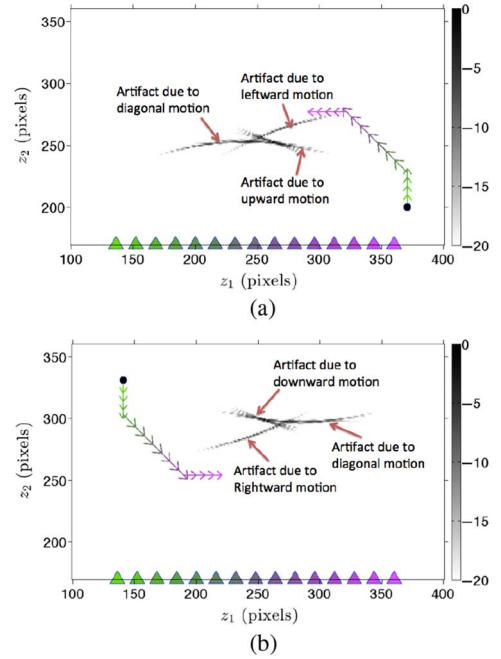


Fig. 12. The reflectivity images of a maneuvering target (a) rotating to the left of the scene and (b) rotating to the right of the scene. The images are reconstructed by overlapping sixteen subapertures. The triangles show the phase centers of the bistatic antennas at the midpoint of the subapertures. The bistatic geometry is the same as in Scenario 2. The solid circle shows the true (initial) location of the target, The arrowed path shows the locations and velocity directions of the target for each subaperture.

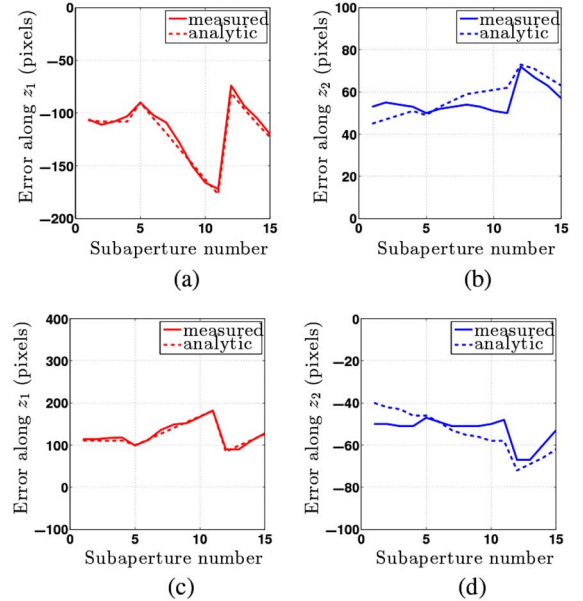


Fig. 13. The measured position errors (solid) and analytic position errors (dashed - calculated from (35a) and (35b)) along x_1 and x_2 directions for different subapertures. The target is rotating to the left and to the right of the scene.

reconstructed images for the two scenes each one with a maneuvering target. In the first scene, the target moves upwards and rotates leftward as shown by the arrowed path in Fig. 12 (a). In the second one, the target moves downward and rotates towards the right as shown by the arrowed path in Fig. 12 (b). The images are reconstructed from fifteen subapertures. Fig. 13 shows the comparison of the measured and analytic position

errors for the maneuvering target in the first scene. The analytic errors are computed using (35a) and (35b) at the end of each subaperture. The images show that as the target velocity changes from vertical to horizontal direction, the moving target morphology changes from displacement to smearing. For the first (between the first and fourth subapertures) and the second maneuver (between the fifth and eleventh subapertures), the radial target velocity causes displacement artifacts in the z_1 direction, as observed in Figures 12(a) and (b) and shown by the error plots in Figures 13 (a) and (c). The artifacts along the z_2 direction are smaller and mostly due to the transverse target velocity component. Note that accurate estimation of these displacements is obscured by the large displacement due to radial target velocity. The effect of transverse target velocity becomes more significant with the third maneuver involving the horizontal target motion causing smearing artifacts along the z_1 direction.

VII. CONCLUSION

We presented an analysis of the positioning errors in SAR imagery due to moving targets. Our analysis is applicable to bistatic and monostatic configurations, extended targets, wide apertures and arbitrary imaging geometries including arbitrary antenna trajectories and target velocities. The analysis provides a parametric set of equations to predict two or three dimensional positioning errors that can explain complex moving target morphology observed in SAR imagery.

We further studied specific geometric configurations and presented corresponding predictive equations for target positioning errors. The first case involves a bistatic configuration with a stationary transmitter. The second case involves a bistatic configuration whereby the transmitter and receiver move in tandem in straight, linear trajectories at a constant height and at a constant velocity. The third case involves monostatic configuration whereby the antenna moves in a straight linear trajectory. The analysis shows that the positioning error in both the radial and transverse directions are primarily determined by the factors scaling the radial target velocity. The radial positioning error is scaled by the length of the aperture. The transverse positioning error is directly proportional to the receiver antenna range, the azimuthal angle and the bistatic elevation angle; and inversely proportional to the antenna speed and the bistatic angle. For the bistatic, short aperture, tandem configuration, the error in the transverse direction is directly proportional to the distance between the antennas. For typical ground moving targets, the transverse positioning error is dominant since antenna ranges are much larger than the distances traveled by ground targets. If a target does not exhibit a radial velocity, the positioning error is observed only in the transverse direction and proportional to the aperture length.

We present numerical simulations to verify our analysis in different scenarios including bistatic and monostatic configurations involving short and long apertures, linear and non-traditional circular and parabolic trajectories. The positioning errors obtained from the simulations are consistent

with the analytical ones predicted by the analysis. We reserve the validation of our results using real images formed using measured SAR data for future work.

The predictive equations describing the positioning errors in arbitrary imaging geometries offer the potential capability to estimate target motion parameters and thereby to form focused images.

The theoretical framework developed in this paper can be used to analyze moving target positioning errors in other SAR modalities, such as Doppler SAR [3], [4], [7] and passive SAR [1], [2], [5], [9], [11], [40], [41].

Our analysis is developed for SAR imaging of ground moving targets; however, the results can be easily extended to imaging of airborne targets. While in the current paper we assumed that the phase errors arise primarily from moving targets, the analysis can be extended to include antenna platform trajectory errors and random phase errors. We leave the investigation of these topics to future research.

Finally, while our primary interest is in radar imaging, our method is also applicable to other tomographic imaging problems such as those that arise in acoustics.

APPENDIX I

Evaluating (15), we have the following equality

$$\Delta \mathbf{z} \cdot \nabla_{\mathbf{z}} [R(s, \mathbf{z}) + B(s, \mathbf{z}, \mathbf{v}_{\mathbf{z}})] = -B(s, \mathbf{z}, \epsilon \Delta \mathbf{v}_{\mathbf{z}}). \quad (43)$$

$\nabla_{\mathbf{z}} R(s, \mathbf{z})$ is given as follows:

$$\nabla_{\mathbf{z}} R(s, \mathbf{z}) = D\psi(\mathbf{z})[(\mathbf{z} - \widehat{\gamma}_R(s)) + (\mathbf{z} - \widehat{\gamma}_T(s))]. \quad (44)$$

$\nabla_{\mathbf{z}} B(s, \mathbf{z}, \mathbf{v}_{\mathbf{z}})$ can be calculated as follows:

$$\begin{aligned} \nabla_{\mathbf{z}}[(\mathbf{z} - \widehat{\gamma}(s)) \cdot \mathbf{v}_{\mathbf{z}} s] = \\ \frac{\nabla_{\mathbf{z}}[(\mathbf{z} - \gamma(s)) \cdot \mathbf{v}_{\mathbf{z}} s] - D\psi(\mathbf{z})(\mathbf{z} - \widehat{\gamma}(s))[(\mathbf{z} - \widehat{\gamma}(s)) \cdot \mathbf{v}_{\mathbf{z}} s]}{|\mathbf{z} - \gamma(s)|}. \end{aligned} \quad (45)$$

Let $\mathbf{z} = [z_1, z_2, \psi(\mathbf{z})]$, $\mathbf{v}_{\mathbf{z}} = [v_1, v_2, \nabla_{\mathbf{z}}\psi(\mathbf{z}) \cdot \mathbf{v}_{\mathbf{z}}]$ and $\gamma(s) = [\gamma_1(s), \gamma_2(s), \gamma_3(s)]$. Then, $\nabla_{\mathbf{z}}[(\mathbf{z} - \gamma(s)) \cdot \mathbf{v}_{\mathbf{z}} s]$ is given as follows:

$$\begin{aligned} \nabla_{\mathbf{z}}[(\mathbf{z} - \gamma(s)) \cdot \mathbf{v}_{\mathbf{z}} s] \\ = \begin{bmatrix} 1 & 0 & \frac{\partial \psi(\mathbf{z})}{\partial z_1} \\ 0 & 1 & \frac{\partial \psi(\mathbf{z})}{\partial z_2} \end{bmatrix} \begin{bmatrix} v_1 \\ v_2 \\ v_3 \end{bmatrix} s + \begin{bmatrix} \frac{\partial^2 \psi(\mathbf{z})}{\partial z_1^2} & \frac{\partial^2 \psi(\mathbf{z})}{\partial z_1 \partial z_2} \\ \frac{\partial^2 \psi(\mathbf{z})}{\partial z_2 \partial z_1} & \frac{\partial^2 \psi(\mathbf{z})}{\partial z_2^2} \end{bmatrix} \begin{bmatrix} v_1 \\ v_2 \end{bmatrix} (\psi(\mathbf{z}) - \gamma_3(s)) s \\ = [D\psi(\mathbf{z})\mathbf{v}_{\mathbf{z}} + H\psi(\mathbf{z})\mathbf{v}_{\mathbf{z}}(\psi(\mathbf{z}) - \gamma_3(s))] s \end{aligned} \quad (46)$$

where H denotes the Hessian

$$H\psi(\mathbf{z}) = \begin{bmatrix} \frac{\partial^2 \psi(\mathbf{z})}{\partial z_1^2} & \frac{\partial^2 \psi(\mathbf{z})}{\partial z_1 \partial z_2} \\ \frac{\partial^2 \psi(\mathbf{z})}{\partial z_2 \partial z_1} & \frac{\partial^2 \psi(\mathbf{z})}{\partial z_2^2} \end{bmatrix} \quad (47)$$

of $\psi(\mathbf{z})$. Plugging (46) into (45), we re-express (45) as:

$$\begin{aligned} & \nabla_{\mathbf{z}}[(\widehat{\mathbf{z} - \gamma(s)}) \cdot \mathbf{v}_{\mathbf{z}}s] \\ &= \frac{[D\psi(\mathbf{z})\mathbf{v}_{\mathbf{z}} + H\psi(\mathbf{z})\mathbf{v}_{\mathbf{z}}(\psi(\mathbf{z}) - \gamma_3(s))]s}{|\mathbf{z} - \gamma(s)|} \\ & \quad - \frac{D\psi(\mathbf{z})(\widehat{\mathbf{z} - \gamma(s)})[(\widehat{\mathbf{z} - \gamma(s)}) \cdot \mathbf{v}_{\mathbf{z}}s]}{|\mathbf{z} - \gamma(s)|}. \end{aligned} \quad (48)$$

Plugging (44) and (48) into the left hand side of (43) we get

$$\begin{aligned} & D\psi(\mathbf{z}) \left[(\widehat{\mathbf{z} - \gamma_R(s)}) + (\widehat{\mathbf{z} - \gamma_T(s)}) \right] - \\ & D\psi(\mathbf{z}) \left[\frac{\mathbf{v}_R^\perp s}{|\mathbf{z} - \gamma_R(s)|} + \frac{\mathbf{v}_T^\perp s}{|\mathbf{z} - \gamma_T(s)|} \right] + \\ & H\psi(\mathbf{z})\mathbf{v}_{\mathbf{z}}s [(\psi(\mathbf{z}) - \gamma_{3R}(s)) + (\psi(\mathbf{z}) - \gamma_{3T}(s))]. \end{aligned} \quad (49)$$

For flat topography $H\psi(\mathbf{z})$ vanishes leading to (17).

APPENDIX II

For the bistatic configuration with stationary transmitter $D\psi(\mathbf{z})\dot{\mathbf{L}}(s, \mathbf{z})$ becomes

$$\begin{aligned} D\psi(\mathbf{z})\dot{\mathbf{L}}(s, \mathbf{z}) &= \frac{D\psi(\mathbf{z})\dot{\gamma}_R^\perp(s)}{|\mathbf{z} - \gamma_R(s)|}, \\ &= \frac{a_1\widehat{\mathbf{L}}_R(s, \mathbf{z}) - a_2D\psi(\mathbf{z})\widehat{\gamma}_R(s)}{|\mathbf{z} - \gamma_R(s)|}, \end{aligned} \quad (50)$$

where $a_1 = |\dot{\gamma}_R(s)| \sin(\Phi_R(s, \mathbf{z})) \cos(\phi_R(s, \mathbf{z}))$ and $a_2 = |\dot{\gamma}_R(s)|$. For the definitions and geometric illustrations of Φ_R and ϕ_R , see Section V-1 and Fig. 1.

Using $\dot{\gamma}_R(s) = [\mathbf{v}_a, 0]$, we write

$$\begin{aligned} |D\psi(\mathbf{z})\dot{\gamma}_R^\perp(s)|^2 &= [(a_1\widehat{\mathbf{L}}_R(s, \mathbf{z}) - a_2\widehat{\mathbf{v}}_a) \cdot (a_1\widehat{\mathbf{L}}_R(s, \mathbf{z}) - a_2\widehat{\mathbf{v}}_a)], \\ &= |a_1|^2 + |a_2|^2 - 2|a_1|a_2|\widehat{\mathbf{L}}_R(s, \mathbf{z}) \cdot \widehat{\mathbf{v}}_a|. \end{aligned} \quad (51)$$

Using $\widehat{\mathbf{L}}_R(s, \mathbf{z}) \cdot \widehat{\mathbf{v}}_a = \cos(\phi_R(s, \mathbf{z})) / \sin(\Phi_R(s, \mathbf{z}))$, and plugging in a_1 and a_2 into (51), we have

$$|D\psi(\mathbf{z})\dot{\gamma}_R^\perp(s)|^2 = |\mathbf{v}_a|^2 \beta_R^2(s, \mathbf{z}), \quad (52)$$

where $\beta_R^2(s, \mathbf{z}) = \sin^2(\phi_R(s, \mathbf{z})) - \cos^2(\phi_R(s, \mathbf{z})) \cos^2(\Phi_R(s, \mathbf{z}))$. Thus,

$$|D\psi(\mathbf{z})\dot{\mathbf{L}}(s, \mathbf{z})| = \frac{|\mathbf{v}_a| |\beta_R(s, \mathbf{z})|}{|\mathbf{z} - \gamma_R(s)|}. \quad (53)$$

For this particular configuration,

$$|D\psi(\mathbf{z})\mathbf{L}(s, \mathbf{z})| = 2 \sin(\Phi(s, \mathbf{z})) \cos(\Theta(s, \mathbf{z})/2), \quad (54)$$

where $\Theta(s, \mathbf{z})$ is the bistatic angle and $\Phi(s, \mathbf{z})$ is the angle between $\mathbf{L}(s, \mathbf{z})$ and the normal vector of the ground plane. Plugging (53) and (54) into (35b), we obtain (37).

APPENDIX III

For the bistatic configuration specified in Section V-2, we have the following expression for $D\psi(\mathbf{z})\dot{\mathbf{L}}$

$$\begin{aligned} D\psi(\mathbf{z})\dot{\mathbf{L}} &= \frac{D\psi(\mathbf{z})\dot{\gamma}_T^\perp(s)}{|\mathbf{z} - \gamma_T(s)|} + \frac{D\psi(\mathbf{z})\dot{\gamma}_R^\perp(s)}{|\mathbf{z} - \gamma_R(s)|}, \\ &= |\mathbf{v}_a| \left[\alpha \widehat{\mathbf{L}} - \left(\frac{1}{|\mathbf{z} - \gamma_T(s)|} + \frac{1}{|\mathbf{z} - \gamma_R(s)|} \right) \widehat{\mathbf{v}}_a \right], \end{aligned} \quad (55)$$

where $\alpha = \alpha_T^2 + \alpha_R^2 + 2\alpha_T\alpha_R \cos(\theta)$ and $\alpha_{T,R} = \sin(\Phi_{T,R}) \cos(\phi_{T,R}) / |\mathbf{z} - \gamma_{T,R}(s)|$.

Please refer to Fig. 2 for the definitions and geometric depictions of the angles θ , Φ_T , ϕ_T and Φ_R , ϕ_R . In (55), the term α is small compared to the second term so it can be ignored. Then, we express the second term in (55) as

$$\begin{aligned} \frac{1}{|\mathbf{z} - \gamma_T(s)|} + \frac{1}{|\mathbf{z} - \gamma_R(s)|} &= \frac{|\mathbf{z} - \gamma_T(s)| + |\mathbf{z} - \gamma_R(s)|}{|\mathbf{z} - \gamma_T(s)||\mathbf{z} - \gamma_R(s)|}, \\ &\approx \frac{2 \sin(\Theta)}{|\mathbf{D}|}, \end{aligned} \quad (56)$$

where $|\mathbf{D}|$ is the distance between the transmitter and the receiver, and Θ is the angle between the transmitter and receiver look-directions. Finally, $D\psi(\mathbf{z})\dot{\mathbf{L}}$ is approximated as

$$D\psi(\mathbf{z})\dot{\mathbf{L}} \approx -\frac{2|\mathbf{v}_a| \sin(\Theta) \widehat{\mathbf{v}}_a}{|\mathbf{D}|}. \quad (57)$$

Plugging (57) and $|D\psi(\mathbf{z})\mathbf{L}| = 2 \sin(\Phi) \cos(\Theta/2)$ into (35b), where Φ is the angle between $\widehat{\mathbf{L}}$ and normal vector of the flat ground, we obtain (42).

REFERENCES

- [1] S. Wacks and B. Yazıcı, "Passive synthetic aperture hitchhiker imaging of ground moving targets part 1: Image formation and velocity estimation," *IEEE Trans. Image Process.*, vol. 23, no. 6, pp. 2487–2500, Jun. 2014.
- [2] S. Wacks and B. Yazıcı, "Passive synthetic aperture hitchhiker imaging of ground moving targets part 2: Performance analysis," *IEEE Trans. Image Process.*, vol. 23, no. 9, pp. 4126–4138, Sep. 2014.
- [3] L. Wang and B. Yazıcı, "Bistatic synthetic aperture radar imaging of moving targets using ultra-narrowband continuous waveforms," *SIAM J. Imag. Sci.*, vol. 7, no. 2, pp. 824–866, 2014.
- [4] L. Wang and B. Yazıcı, "Ground moving target imaging using ultranarrowband continuous wave synthetic aperture radar," *IEEE Trans. Geosci. Remote Sens.*, vol. 51, no. 9, pp. 4893–4910, Sep. 2013.
- [5] L. Wang, C. E. Yarman, and B. Yazıcı, "Doppler-hitchhiker: A novel passive synthetic aperture radar using ultranarrowband sources of opportunity," *IEEE Trans. Geosci. Remote Sens.*, vol. 49, no. 10, pp. 3521–3537, Oct. 2011.
- [6] K. Voccola, M. Cheney, and B. Yazıcı, "Polarimetric synthetic-aperture inversion for extended targets in clutter," *Inverse Prob.*, vol. 29, no. 5, pp. 054003, 2013.
- [7] L. Wang and B. Yazıcı, "Bistatic synthetic aperture radar imaging using ultranarrowband continuous waveforms," *IEEE Trans. Image Process.*, vol. 21, no. 8, pp. 3673–3686, Aug. 2012.
- [8] V. Krishnan and B. Yazıcı, "Synthetic aperture radar imaging exploiting multiple scattering," *Inverse Prob.*, vol. 27, no. 5, pp. 055004, 2011.
- [9] C. E. Yarman, L. Wang, and B. Yazıcı, "Doppler synthetic aperture hitchhiker imaging," *Inverse Prob.*, vol. 26, no. 6, pp. 065006, 2010.
- [10] V. Krishnan, J. Swoboda, C. E. Yarman, and B. Yazıcı, "Multistatic synthetic aperture radar image formation," *IEEE Trans. Image Process.*, vol. 19, no. 5, pp. 1290–1306, May 2010.

- [11] C. E. Yarman and B. Yazıcı, "Synthetic aperture hitchhiker imaging," *IEEE Trans. Image Process.*, vol. 17, no. 11, pp. 2156–2173, Nov. 2008.
- [12] C. E. Yarman, B. Yazıcı, and M. Cheney, "Bistatic synthetic aperture radar imaging for arbitrary flight trajectories," *IEEE Trans. Image Process.*, vol. 17, no. 1, pp. 84–93, Jan. 2008.
- [13] B. Yazıcı, M. Cheney, and C. E. Yarman, "Synthetic-aperture inversion in the presence of noise and clutter," *Inverse Prob.*, vol. 22, no. 5, pp. 1705, 2006.
- [14] C. J. Nolan and M. Cheney, "Microlocal analysis of synthetic aperture radar imaging," *J. Fourier Anal. Appl.*, vol. 10, pp. 133–148, 2004.
- [15] S. Nilsson, Application of fast backprojection techniques for some inverse problems of integral geometry, Ph.D. dissertation, Studies in Science and Technology, Linköping Univ., Linköping, Sweden, 1997.
- [16] B. Yazıcı and V. Krishnan, "Microlocal analysis in imaging," 2010 [Online]. Available: http://www.ecse.rpi.edu/~yazici/ICASSPTutorial/microlocal_ICASSP10.html
- [17] R. K. Raney, "Synthetic aperture imaging radar and moving targets," *IEEE Trans. Aerosp. Electron. Syst.*, vol. 7, no. 3, pp. 499–505, May 1971.
- [18] N. Marechal, R. Dickinson, and G. Karamyan, "A 2D wavenumber domain phase model for ground moving vehicles in synthetic aperture radar imagery," *Inverse Prob.*, vol. 29, no. 5, pp. 054010, 2013.
- [19] L. M. H. Ulander and H. Hellsten, "Low-frequency ultrawideband array antenna SAR for stationary and moving target imaging," *Proc. SPIE*, vol. 3704, pp. 149–158, 1999.
- [20] A. F. Yegulalp, "Analysis of SAR image formation equations for stationary and moving targets," MIT Lincoln Laboratory, Lexington, MA, USA, Tech. Rep. FPR-14, 2002.
- [21] J. K. Jao and A. F. Yegulalp, "Multichannel synthetic aperture radar signatures and imaging of a moving target," *Inverse Prob.*, vol. 29, no. 5, pp. 054009, 2013.
- [22] D. A. Garren, "Smear signature morphology of surface targets with arbitrary motion in spotlight synthetic aperture radar imagery," *IET Radar Sonar Navigat.*, vol. 8, no. 5, pp. 435–448, 2014.
- [23] R. P. Perry, R. C. Dipietro, and R. L. Fante, "SAR imaging of moving targets," *IEEE Trans. Aerosp. Electron. Syst.*, vol. 35, no. 1, pp. 188–200, Jan. 1999.
- [24] J. R. Fienup, "Detecting moving targets in SAR imagery by focusing," *IEEE Trans. Aerosp. Electron. Syst.*, vol. 37, pp. 794–801, Jul. 2001.
- [25] D. Cristallini, D. Pastina, F. Colone, and P. Lombardo, "Efficient detection and imaging of moving targets in SAR images based on chirp scaling," *IEEE Trans. Geosci. Remote Sens.*, vol. 51, no. 4, pp. 2403–2416, Apr. 2013.
- [26] V. T. Vu, T. K. Sjogren, M. I. Pettersson, A. Gustavsson, and L. M. H. Ulander, "Detection of moving targets by focusing in UWB SAR—Theory and experimental results," *IEEE Trans. Geosci. Remote Sens.*, vol. 48, no. 10, pp. 3799–3815, Oct. 2010.
- [27] C. V. Jakowatz, J. D. E. Wahl, and P. H. Eichel, "Refocus of constant velocity moving targets in synthetic aperture radar imagery," in *Proc. SPIE Conf. Algorithms SAR Imagery V*, 1998, vol. 3370, pp. 85–95.
- [28] B. D. Rigling, "Image-quality focusing of rotating SAR targets," *IEEE Trans. Geosci. Remote Sens. Lett.*, vol. 5, no. 4, pp. 750–754, Oct. 2008.
- [29] Y. Ding, N. Xue, and D. C. Munson, "An analysis of time-frequency methods in SAR imaging of moving targets," in *Proc. Sensor Array Multichannel Signal Process. Workshop*, Cambridge, MA, USA, Mar. 2000, pp. 221–225.
- [30] Y. Ding and D. C. Munson, "Time-frequency methods in SAR imaging of moving targets," in *Proc. IEEE Int. Conf. Acoust., Speech Signal Process.*, Orlando, FL, USA, May 2002, pp. 2881–2884.
- [31] J. K. Jao, "Theory of synthetic aperture radar imaging of a moving target," *IEEE Trans. Geosci. Remote Sens.*, vol. 39, pp. 1984–1992, Sep. 2001.
- [32] G. Li, J. Xu, Y. N. Peng, and X. G. Xia, "Bistatic linear antenna array SAR for moving target detection, location, and imaging with two passive airborne radars," *IEEE Trans. Geosci. Remote Sens.*, vol. 45, no. 3, pp. 554–565, Mar. 2007.
- [33] M. J. Minardi, L. A. Gorham, and E. G. Zelnio, "Ground moving target detection and tracking based on generalized SAR processing and change detection," *Proc. SPIE*, vol. 5808, p. 156, 2005.
- [34] F. Zhou, R. Wu, M. Xing, and Z. Bao, "Approach for single channel SAR ground moving target imaging and motion parameter estimation," *IET Radar Sonar Navigat.*, vol. 1, no. 1, pp. 59–66, Sep. 2007.
- [35] S. Zhu, G. Liao, Y. Qu, Z. Zhou, and X. Liu, "Ground moving targets imaging algorithm for synthetic aperture radar," *IEEE Trans. Geosci. Remote Sens.*, vol. 49, no. 1, pp. 462–477, 2011.
- [36] M. Martorella, F. Berizzi, E. Giusti, and A. Bacci, "Refocusing of moving targets in SAR images based on inversion mapping and ISAR processing," in *Proc. IEEE Int. Radar Conf.*, Kansas City, MO, USA, 2011, pp. 68–72.
- [37] M. Martorella, F. Berizzi, and B. Haywood, "Contrast maximisation based technique for 2D ISAR autofocusing," in *Proc. IEE Radar Sonar Navigat.*, Aug. 2005, vol. 152, pp. 253–262.
- [38] S. Werness, W. Carrara, L. Joyce, and D. Franczak, "Moving target imaging algorithm for SAR data," *IEEE Trans. Aerosp. Electron. Syst.*, vol. 26, no. 1, pp. 57–66, Jan. 1990.
- [39] D. E. Hack and M. A. Saville, "Analysis of SAR moving grid processing for focusing and detection of ground moving targets," in *Proc. SPIE Defense, Security Sens.*, Orlando, FL, USA, Apr. 2011, vol. 8051, p. 80510S.
- [40] L. Wang and B. Yazıcı, "Passive imaging of moving targets exploiting multiple scattering using sparse distributed apertures," *Inverse Prob.*, vol. 28, no. 12, pp. 125009, 2012.
- [41] L. Wang and B. Yazıcı, "Passive imaging of moving targets using sparse distributed apertures," *SIAM J. Imag. Sci.*, vol. 5, no. 3, pp. 769–808, 2012.
- [42] W. Q. Wang and H. Shao, "Two-antenna SAR with waveform diversity for ground moving target indication," *IEEE Trans. Geosci. Remote Sens.*, vol. 11, no. 12, pp. 2154–2158, Dec. 2014.
- [43] K. Duman and B. Yazıcı, "Ground moving target imaging using bistatic synthetic aperture radar," in *Proc. IEEE Radar Conf. (RADAR'13)*, 2013, pp. 1–4.
- [44] F. Trèves, *Introduction to Pseudodifferential and Fourier Integral Operators: Vol. 2: Fourier Integral Operators*. New York, NY, USA: Plenum, 1980.
- [45] F. Trèves, *Introduction to Pseudodifferential and Fourier Integral Operators: Vol. 1: Pseudodifferential Operators*. New York, NY, USA: Plenum, 1982.
- [46] H. C. Yank, Z. Li, and B. Yazıcı, "Computationally efficient FBP-type direct segmentation of synthetic aperture radar images," in *Proc. SPIE Defense Security Sens.*, 2011, pp. 80510C–80510C.
- [47] H. C. Yank, "Analytic methods for SAR image formation in the presence of noise and clutter," Ph.D. dissertation, School Eng., Rensselaer Polytechnic Inst., Troy, NY, USA, 2014.
- [48] L. Hörmander, *The Analysis of Linear Partial Differential Operators: Vol. 1.: Distribution Theory and Fourier Analysis*. Berlin, Germany: Springer-Verlag, 1983.



Kaan Duman (S'15) received the B.Sc. and M.Sc. degrees in electrical and electronics engineering from Bilkent University, Ankara, Turkey, in 2007 and 2010, respectively. He is currently pursuing the Ph.D. degree in electrical engineering at Rensselaer Polytechnic Institute, Troy, NY, USA.



Birsan Yazıcı (M'94–SM'06) received the B.S. degree in electrical engineering and mathematics from Bogazici University, Istanbul Turkey, in 1988, and the M.S. and Ph.D. degrees in mathematics and electrical engineering from Purdue University, West Lafayette, IN, USA, in 1990 and 1994, respectively. From September 1994 until 2000, she was a Research Engineer with General Electric Company Global Research Center, Schenectady, NY, USA. During her tenure in industry, she worked on radar, transportation, industrial and medical imaging systems. From 2001 to June 2003, she was an Assistant Professor with the Department of Electrical and Computer Engineering, Drexel University, Philadelphia, PA, USA. In Fall 2003, she joined Rensselaer Polytechnic Institute, Troy, NY, USA, where she is currently a Full Professor with the Department of Electrical, Computer, and Systems Engineering and the Department of Biomedical Engineering. She holds 11 U.S. patents. Her research interests include the areas of statistical signal processing, inverse problems in imaging, image reconstruction, biomedical optics, radar and X-ray imaging. She served as an Associate Editor for the IEEE TRANSACTIONS ON IMAGE PROCESSING from 2008 to 2012 and for *SIAM Journal on Imaging Science* from 2010 to 2014. She currently serves as an Associate Editor for IEEE TRANSACTIONS ON GEOSCIENCES AND REMOTE SENSING. She was the recipient of the Rensselaer Polytechnic Institute 2007 and 2013 School of Engineering Research Excellence Awards.